Gold nanoparticle self-assembly as means for making electrocatalysts and magnetic nanonets and their application for oxygen evolution reaction and water purification

by

Venkatesh Sanjeevan Guruprasad

A thesis

presented to the University of Waterloo

in fulfilment of the

thesis requirement for the degree of

Master of Science

in

Chemistry (Nanotechnology)

Waterloo, Ontario, Canada, 2018

Author’s Declaration

I hereby declare that I am the sole author of this thesis. This is a true copy of the thesis, including any required final revisions, as accepted by my examiners.

I understand that my thesis may be made electronically available to the public.

Abstract

Gold nanoparticles (AuNPs) are widely researched materials in nanotechnology due to their distinct properties like surface plasmon resonance and ability to self-assemble. Citrate capped gold nanoparticles assembled into chains using multivalent cations are used for multiple applications such as sensing, water purification and catalysis; hence their study is of importance. Knowledge of the parameters which affect self-assembly will help to optimize and control the self-assembly process. We research using various experimental techniques how the self-assembly depends on ionic strength, the dissociation constant of the citrate and the type of ion used for the assembly process.

Self-assembly of Au nanoparticles with Fe ions (Fe^{2+}/Fe^{3+} in 1:2 molar ratio) is used to develop magnetic nano-nets similar to fishing nets for capture and removal of microbes in aqueous medium. The nano-nets have a high aspect ratio, span microns in length with openings of 80-300 nm. This allows them to sample the liquid medium even at low volume fraction and also entrap the microbes in the solution. The nets and the trapped microbes can be effectively pulled from the solution by using an off the shelf magnet. Since the capture is based on physical contact, the nano-nets overcome the ability of the microbes to develop resistance to the cytotoxic effects of chemical compounds and nanomaterials. Using the nano-nets an absolute inactivation of 0.9 is achieved in 5 min. in a non-deaerated solution with Escherichia coli (E. coli). Further the removal of the nano-nets along with the captured microbes also predominantly eliminates the nanomaterial from the aqueous medium for future use.

Further, we research the catalytic properties of self-assembled Au cobalt oxide chains for the Oxygen Evolution Reaction which is a half reaction of water splitting. Micron sized branched

3-D networks of AuNP are formed with cobalt oxide linkers. The self-assembled structures help to effectively disperse the catalyst and provide an easy fabrication process for our catalyst. The gold template enhances the conductivity of our cobalt oxide catalyst due to the formation of conductive gold chains. In addition, our catalyst exhibits low overpotential of 430 mV (at 10 mA/cm^2 current density), high turnover frequency (TOF) of 0.07 s^{-1} (at 400 mV overpotential) and a very low Tafel slope of 30 mV/dec as compared to many previous works. Stability of our catalyst has also been evaluated.

Acknowledgements

Firstly, I would like to express my deepest gratitude to my supervisor, Professor Vivek Maheshwari, for giving me the opportunity to work in his group and for guiding me throughout my graduate study. His expertise, insights and patience have led me to solve all the problems that I have encountered.

I would like to also thank all my committee members: Professor Juewen Liu and Professor Anna Klinkova for being on my committee and giving me valuable feedback at each stage.

Special thanks go to my colleagues and friends: Rohit Saraf and Maarij Baig. We have spent countless hours working together in the lab and it was my pleasure to work with you. I would like to also thank other colleagues in the lab: Hua Fan, Shehan Salgado and Avi Mathur for their support.

Finally, I would like to acknowledge the support from my family. It was their love and care which gave me the strength and courage to pursue my goals.

Table of Contents

List of figures

List of abbreviations

Abbreviations	Full names
LSV	Linear sweep voltammetry
AuNP	Gold nanoparticles
FESEM	Field emission scanning electron microscopy
TEM	Transmission electron microscopy
UV-Vis	Ultraviolet visible spectroscopy
XPS	X-ray photoelectron spectroscopy
DLS	Dynamic light scatter
GCE	Glassy carbon electrode
GIXRD	Grazing incidence x-ray diffraction
SPR	Surface plasmon resonance
3-D	Three dimensions
1-D	One dimension
CNT	Carbon nanotubes
CFU	Colony forming units
PMMA	Poly(methyl methacrylate)
OER	Oxygen evolution reaction
HER	Hydrogen evolution reaction
TOF	Turnover frequency

Thesis organization

This thesis is divided into four chapters.

Chapter 1 of this thesis is about the self-assembly of gold nanoparticles

Chapter 2 of this thesis is about the application of self-assembled gold nanoparticle chains for the capture of bacteria and microspheres more than 100 nm in size. AuNP-FeO_x composite chains are made which act as magnetic nano-nets for the capture of bacteria.

Chapter 3 of this thesis is about the application of self-assembled gold nanoparticle chains as an electrocatalyst for the water splitting reaction. AuNP-CoO composite chains are made which shows good catalytic response for the water splitting reaction.

Chapter 1: Gold nanoparticle self-assembly

Introduction

AuNPs are widely researched nanomaterials in recent times.[1–6] Nanoparticles are defined as particles with sizes between about 1 and 100 nm that show properties that are not found in bulk samples of the same material. AuNPs can be synthesized with control over its sizes.[7] We use 10-12 nm (diameter) spherical nanoparticles for our research since standard solutions are readily available which facilitates repeatable research. As stable metal nanoparticles, AuNPs possess fascinating properties including self-assembly, size-related electronic and optical characteristics.[8,9]

Gold is a precious material and historically has been used in making ornaments, coloured glass and medicine. AuNPs are significant because they exhibit unique optical properties which can be used for sensing, imaging, biological and catalysis applications.[9] They will be a key material in the 21st century and are important materials in bottom-up nanotechnology applications. The AuNP used in our experiments are synthesized by one of the modified citrate reduction methods, the first of which was reported by Turkevitch in 1951.[10] Colloidal solutions of AuNP of different sizes exhibit different colours as shown in Fig 1.1.[11] The colour of AuNPs is due to collective electron oscillations in the conduction band of the AuNPs which are known as surface plasmon oscillations. These oscillations are in the visible region for AuNPs and hence a strong surface plasmon resonance absorption is observed.[12] The absorption spectra can be measured using a UV-visible spectrophotometer (UV-Vis). When light is incident on the AuNPs, it couples with the surface plasmons and it resonates, which results in a decrease in the intensity of the light which is transmitted after coupling with the surface plasmons. Hence light which

initially was white or having all wavelengths now starts losing a spectrum due to surface plasmon resonance (SPR) and the gold colloid appears coloured. Since the electronic band structure depends on the size and shape of the AuNPs, different sized and shaped particles absorb and reflect light of a different wavelength. In practice, self-assembled chains are blue in colour while the isolated nanoparticles are red in colour due to the coupling of surface plasmons in adjacent particles. This is because in chains there is a change in shape of the electron cloud along the chain which leads to a different SPR as compared to a spherical nanoparticle and hence a different wavelength of absorption.[13]

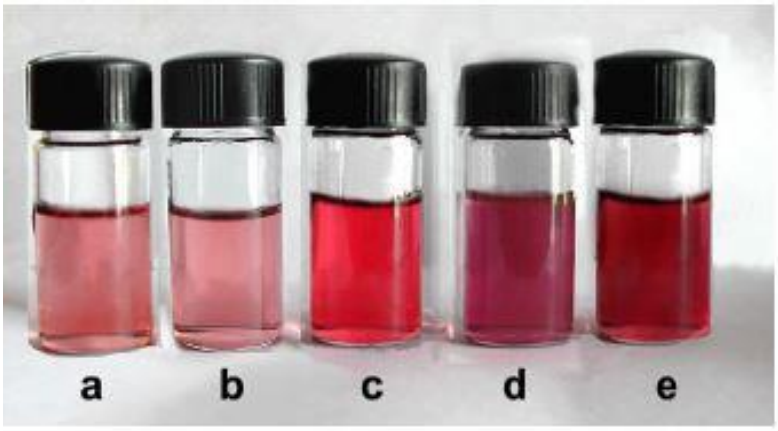

Figure 1.1 Photographs of gold colloids (a) 3 nm, (b) 4 nm, (c) 6 nm, (d) 9 nm, (e) 35 nm in diameter.

Without complex patterning process, self-assembly has been reported to be an easy and cost-effective method to organize nanoparticles into chains. The citrate capped AuNPs with a zeta potential of -32 mV, can be linked to other metal cations such as Ca^{2+}, Mg^{2+}, etc, and self-assemble into chains due to electrostatic forces. In Fig 1.2. are shown the Transmission electron microscopy (TEM) images of self-assembled AuNP with the help of Ca^{2+} linker. If the concentration of the linker ion is too low, it does not form any chains whereas when the

concentration is too high, then the chains aggregate and precipitate. The capping agent which originally is used to keep the gold colloid stable, can be used to self-assemble the particles into branched chains (branched three dimensional (3-D) networks) with the help of a linker ion. The assembly process is monitored both visually due to observable colour change and through UV-Vis measurements. The UV-vis wavelength of peak absorbance redshift as the assembly process progresses as discussed earlier due to surface plasmon resonance coupling.

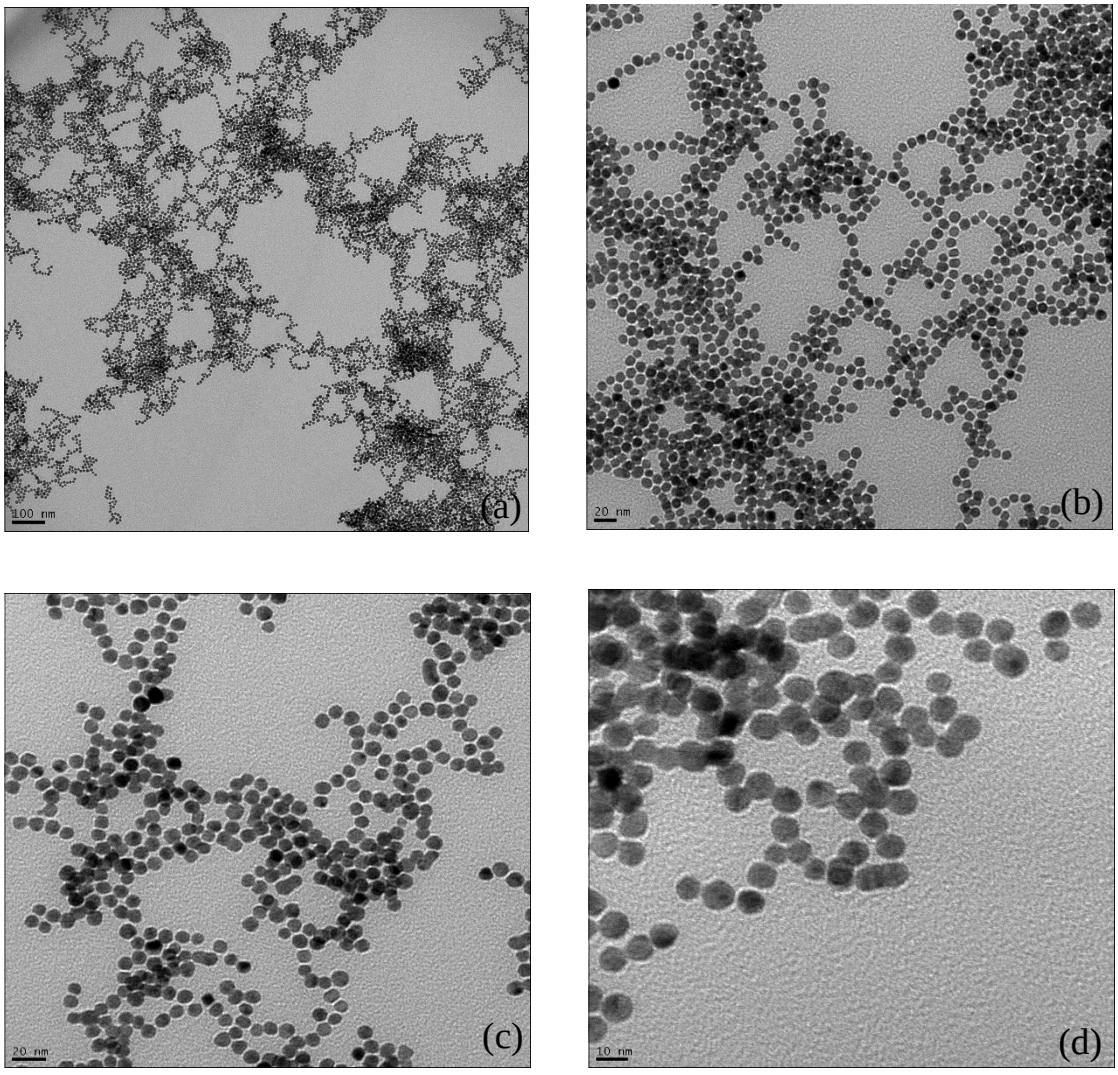

Figure 1.2 (a), (b), (c), (d) Self-assembled AuNP chains assembled with Ca^{2+} ion as linker (0.59mM Ca^{2+} with citrate capped AuNP self-assembled for 8 hours)

Nanoparticles are used as individual entities as well as building blocks of self-assembled structures. Self-assembly of nanoparticles is a result of various forces namely attractive Van der waals forces (V_{vdw}), attractive or repulsive electrostatic forces (V_{elec}) and dipolar (V_{dipole}) interactions.[14] These forces can lead to either dense and close packed clusters or extended crystals. The assembled structures are a result of the balance between these forces. Electrostatic forces are isotropic in nature while dipolar forces are anisotropic. Studies show that for a material to be self-assembled anisotropically into 3-D branched chains, anisotropic forces like dipolar interactions are induced by changing the isotropic electrostatic interactions.[14] By capping the nanoparticles (AuNP) with molecular ligands (like citrate) to minimize the van der Waals attractions and induce dipolar interactions, it has been made recently possible to tune the anisotropic interactions that dominate the self-assembly process, thus leading to anisotropic self-assembly of the nanoparticles into 3-D branched chain like structures. Calculations based on forces in solution shows that the electrostatic forces between the self-assembled structure at its end (V^{end}) is less than that of its side (V^{side}). Hence the growth proceeds at the end of the chain as supposed to the side of the chain.[14] This is illustrated in Fig 1.3. Electron density which is the number of electrons in an ion per volume of ion can play a significant role in contributing to the dipolar interactions which contributes to self-assembly.

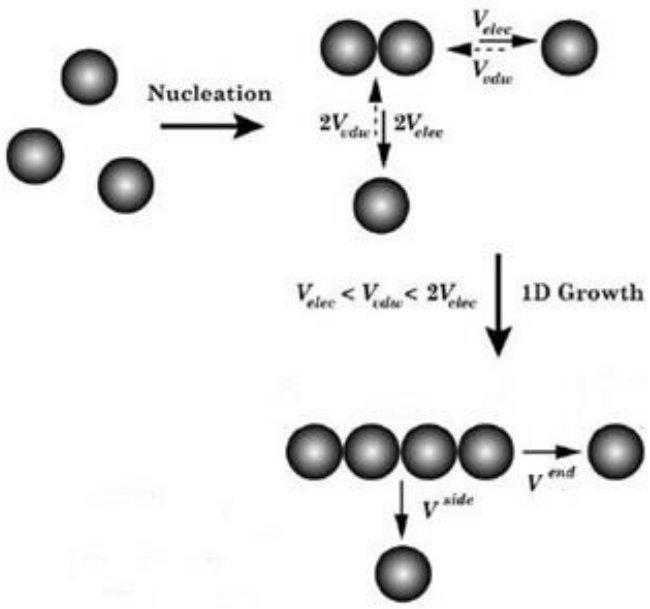

Figure 1.3 Self-assembly of charged nanoparticles showing forces acting on the particles[14]

However, the control of self-assembly has been scarcely studied, especially the self-assembly of AuNP. The various applications of AuNP self-assembled structures have prompted the need to study the methods to control their self-assembly.

In our work we study the different monovalent and divalent cation linkers for the self-assembly of AuNP (Chapter 1). We use self-assembled AuNP for capture and neutralization of microbes (Chapter 2) due to their branched net structure and for electrocatalysis applications (Chapter 3). The self-assembled structures help to effectively disperse the materials and provide an easy fabrication process for our materials.

Materials and methods

Synthesis

Gold nanoparticles were purchased from BBI International. The citrate capped nanoparticles with around 10-12 nm in diameter, $5.7x10^{12}$ particles/ml are stably suspended in water. These AuNPs have a zeta potential of ~ -32 mV due to the citrate capping on their surface. The salts $CaCl_2$, $MgCl_2$, $FeCl_3$, $FeCl_2$, NaCl, $MnCl_2$, $NiCl_2$, $CuCl_2$, $ZnCl_2$ and $CoCl_2$ were purchased from Sigma-Aldrich.

All the glass vials, caps, pipette tips and Millipore water were autoclaved to sterilize the equipment for elimination of any possible contaminants. A fixed amount of each salt after making them into a solution of known concentration with water was added to 2.0 mL of the stock Au nanoparticles. The final solution was put on a vortex mixer for assembling of Au nanoparticles. As a result of the interaction between the cations and citrate groups the nanoparticles assemble into branched chain like structures. As the 10 nm Au nanoparticles were self-assembled with the cations to form larger nanoparticle chains, the solution mixture became blue in color. The color change was caused by the shift of SPR: oscillating electric field of a light ray interact with the free electrons near a colloidal nanoparticle, leading to a concerted oscillation of electron charge resonance with the frequency of visible light. When particle size increases, the wavelength of the SPR absorption shifts to longer wavelengths. The time of assembly was recorded as the time it would take for the SPR absorption peak to not redshift further and remains fixed at ~627 nm. The Dynamic light scatter (DLS) is used to measure the size of the chains (hydrodynamic radius).

Characterization

Ultraviolet-visible spectroscopy was carried out by using MINI-D2T deuterium tungsten light source and USB4000 Miniature fiber optic spectrometer from Ocean Optics.

Zeta Sizer Nano ZS90 from Malvern Instruments was used for measuring both zeta potential and size distribution of our samples.

Results and discussion

Below table shows the variation in the concentration required for assembly of AuNP along with the time taken for assembly on the addition of each of the following cation. There is also a variation in the final average size observed of the formed nanoparticle chains. We study the relationship between parameters, such as electron density, pK and hydration radius of the ions which affect the amount of cations needed, time of assembly and size of the self-assembled chains.

Cation	r_h (A)	pK	e-density (*10^{30}) m^{-3}	amount of cations needed (mM)	time(min)	size(nm)	Electronic configuration	Ionic radius(pm)
Fe^{2+}	4.28	1.82	50.5	1.23	30	153	1s2 2s2 2p6 3s2 3p6 3d6	78
Mn^{2+}	4.38	1.59	40.2	1.05	90	262	$1s^2 2s^2 2p^6 3s^2 3p^6 3d^5$	83
Zn^{2+}	4.3	2.68	69.1	1.17	105	305	1s2 2s2 2p6 3s2 3p6 3d10	74

Ni^{2+}	4.04	2.56	79.1	1.18	105	290	1s2 2s2 2p6 3s2 3p6 3d8	69
Co^{2+}	4.23	2.68	60.5	1.26	120	270	1s2 2s2 2p6 3s2 3p6 3d7	74.5
Mg^{2+}	4.28	0.84	26.8	0.81	150	243	1s2 2s2 2p6	72
Cu^{2+}	4.19	2.22	69.4	1.49	160	360	1s2 2s2 2p6 3s2 3p6 3d9	73
Ca^{2+}	4.12	1.05	18	0.59	480	200	1s2 2s2 2p6 3s2 3p6	100
Na^{+}	3.58	5.33	9.4	34.20	1400	338	1s2 2s2 2p6	102
Pt^{4+}	4.75	-	295	3.75	2800	300	[Xe] 4f14 5d6	63

Table 1.1. Ion assembly parameters with AuNP

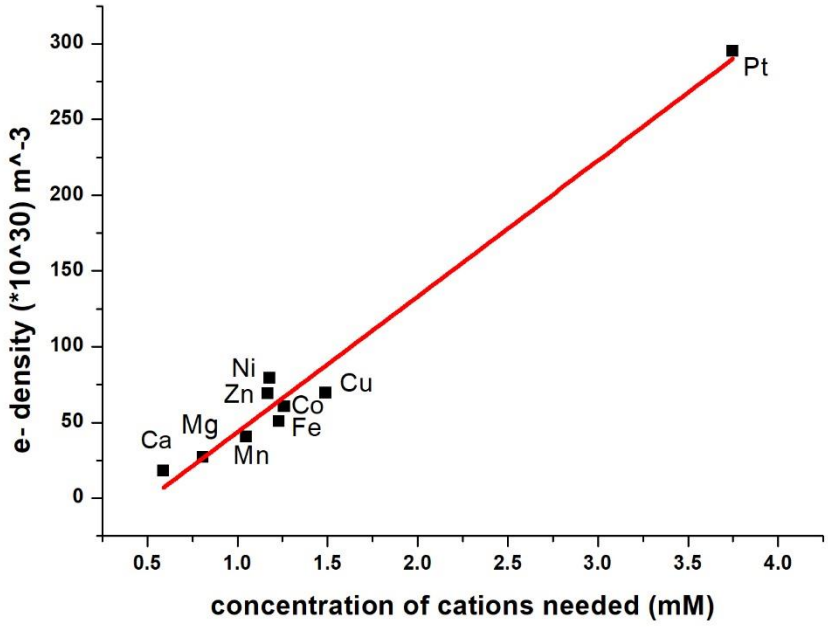

Figure 1.4 Plot of relation between electron density and concentration of cations needed for self-assembly

A general trend which is observed is that as the electron density increases, the amount of ions required increases as shown in Fig 1.4. A point to note is that monovalent ion such as Na^+ requires more than an order of magnitude higher concentration to cause the assembly of the AuNPs. We do not further explore monovalent cations as they need high concentration to self-assemble due to their high pK values and are not applied for any further application. This leads us to stipulate that ionic strength of the solution is not the governing factor for self-assembly. The electron density is given by the total number of electrons in the ion per volume of the ion. The volume of the ion is calculated using ionic radius. The hydration radius is almost a constant with the variation in nature of ion. There is no trend observed in the ionic radius of the ions. pK in Table 1.1 refers to the first dissociation constant of the citrate ion. The pK does not show a significant correlation to either amount of cation or size. The values of hydration radius, pK and electron density are obtained from the literature.[15–18]

Conclusion

AuNPs are widely researched materials in nanotechnology due to their distinct properties like SPR and self-assembly. It has been shown through this work that citrate capped AuNPs can be assembled into chains using cationic linkers which have been used in water purification and electrocatalytic applications. Knowing the parameters which affect self-assembly will help to optimize and control the self-assembly process. We find through this work that the self-assembly of ions is a phenomenon dependent on the type of ion used as the linker and its electron density. In specific the electron density of the ion is directly proportional to the amount of cationic linker needed for self-assembly. This is so because the electron density which is the number of electrons in an ion per volume of ion can play a significant role in contributing to the dipolar interactions as a result of which more cations are needed to balance these forces. A higher electron density will shield the charge on the metal cation more effectively and hence reduce its ionic interaction with the citrate groups on the surface of the Au nanoparticles.

Chapter 2: Magentic nano-nets for capture of microbes in solution based on physical contact

Introduction

Water covers almost seventy percent of the world's surface. Out of this only four percent is freshwater but even of this only one percent is accessible for human consumption. There are still challenges in using this water for human consumption since water is the most common breeding place for a lot of pathogens. Bacterial presence in water is the main indication of contamination. In countries such as India, around eighty percent of diseases are due to bacterial contamination of drinking water. The World Health Organization recommends that potable water should be free from any contamination of coliforms and the presence of faecal matter. Steps must be taken if bacterial contamination is found in water.[19]

Effective neutralization of microbes in water either by capture or by cytotoxic agents is hence of critical importance to prevent diseases.[20] This has gained further urgency due to the spread of bacterial resistance to antibiotics and increasing scarcity of access to clean water.[21–27] Antibiotics have been used for preventing and curing bacterial infections for a long time due to their cost efficiency and powerful outcome. An antimicrobial is a substance which kills microbes or stops their growth. Physical and chemical methods can be used as antimicrobial methods. Chemical antimicrobials are of many types, namely, antibacterial, antifungal, antiviral, antiparasitic agents. Physical methods include heat and radiation treatments. Of the chemical methods nanoparticles of Ag, Fe, Au and Fe-oxides are antimicrobial due to generation of oxidative stresses, disruption of cell membranes and cellular processes, and have been extensively researched for this purpose.[28–38] There has been a need to explore nanomaterials for

antimicrobial purposes since there is an increasing concern that bacteria are developing resistance to antibiotics. The use of these nanoparticles has also been shown to enhance the effect of antibiotics on bacteria through synergy.[39–41] Bacteria are the major cause of chronic and mortal infections in humans. Nanoparticles are increasingly being used to counter bacteria instead of antibiotics.

A rising challenge now is the reported development of microbial resistance to the cytotoxic effects of these nanomaterials.[42] A recent study conducted by Aleš Panáček et al. discussed the bacterial resistance to Ag nanoparticles and strategies to overcome it. One of the mechanisms by which the bacteria develop resistance to Ag nanoparticles may involve the conversion of the cytotoxic Ag^+ species to the less toxic neutral Ag species. The other mechanism proposed is based on the production of the bacterial protein flagellum which agglomerates the AgNP thereby supressing their antibacterial effect. Therefore, nanomaterials that interact and capture the microbes with efficacy by employing alternative strategies are required. To this effect, here we present the use of magnetic nano-nets that are made of Au nanoparticle chains cemented together with Fe-oxides for effective capture of microbes. Unlike 0-Dimensional nanoparticles, these nano-nets have high aspect ratio geometry, which spans microns in size with openings in the range of 80-300 nm. The combined magnetic characteristics of these nets and their ability to sample a greater volume leads to capture of the microbes with great efficacy and also their collection using an off the shelf magnet. Further due to the cytotoxic effects of the constituting materials (Fe oxides) the captured microbes in these nets are also neutralized. These nano-nets effectively combine the physical capture of the microbes due to their geometry with the microbicidal properties of their constituting materials. The removal of

these nano-nets from the solution along with the captured microbes also clears the residual water of the nanomaterial which may have adverse effects on its subsequent use.[43,44]

There are several types of high aspect ratio nanomaterials which have been developed for various applications. The common shapes are nanotubes, nanorods and nanowires. These can be functionalized and have been applied for a variety of applications such as separation of biomolecules, and sensing of biomolecules like glucose and proteins, solar cells, catalysis and electronics. The dimensionality of nanomaterial (and aspect ratio) is a basic physical parameter that critically affects their interaction volume in composites and fluids. For example, the percolation threshold of one dimensional (1-D) materials such as Carbon nanotubes (CNT's) is orders of magnitude smaller than that of spherical nanoparticles.[45,46] The effect of aspect ratio is also seen in thermal conductivity of fluids and composites with nanomaterials as fillers.[47,48] Similar to the effects seen in these processes and parallel to fishing nets used for capture of aquatic organisms, the developed nano-nets function as an effective means for both physical capture and cytotoxic effects induced neutralization of the microbes. Since the nanomaterial developed has a branched chain like 3-D structure with high aspect ratio, it can span large volumes and physically capturing the microbes in the solution in its path. The neutralization of microbes using nanomaterials can be considered a two-step process. First there has to be a direct contact (or close proximity) between the microbe and the nanomaterial in the fluid environment. Success in this step is required for both physical capture of the microbe and also to induce cytotoxic effect on the microbe. The second step is the nanomaterials inducing the cytotoxic effects on the microbe as a result of the direct contact or close proximity. The effect of having a net like nanomaterial is two fold; first due to its high aspect ratio even a small volume fraction of the nets is able to sample a large volume in water, similar to the percolation effects in

composites.[45,46] This greatly increases the probability of contact between the microbe and the nets, satisfying the first step for capture of the microbe. Second as the material is organised into a large network, the interactions with the microbes are at a greater scale than compared with those of single nanoparticles.

We show that using these magnetic nano-nets E. coli in the concentration of $1.6x10^6$ colony forming units (CFU) can be removed from solutions in less than 5 min with more than 90% efficiency. Further the capturing ability of these nano-nets based on their volume fraction in solution and the number density of the target species is characterized using 1 micron Poly(methyl methacrylate) (PMMA) microspheres and also E. coli. By using Au nanoparticles, the minimum size of particles that can be effectively captured by the nano-nets is found to be 100 nm. Also we show their effectiveness in capturing microbes with different physiology by using a mixture of E. coli (a prokaryotic gram negative bacteria) and Saccharomyces Cerevisiae (S. cerevisiae, bakers yeast, a eukaryotic microbe) in water and also towards Bacillus Subtilis (a prokaryotic gram positive bacteria).

Materials and methods

Materials

E. coli strain ATCC 47046, Saccharomyces cerevisiae (yeast) BY4741 are purchased from ATCC. Bacillus Subtilis (Strain 168) was kindly supplied by Prof. Trevor Charles group at University of Waterloo. Au nanoparticles (10 nm with concentration $5.7x10^{12}$ particles/ml; 50 nm with concentration $4.5x10^{10}$ particles/ml and 100 nm with concentration $5.6x10^{9}$ particles/ml) were purchased from Ted Pella (unconjugated gold colloid manufactured by BBI International). Yeast Extract-Pepton-Dextrose (YPD) broth and Nutrient broth No. 1 were purchased from Sigma-Aldrich. $FeCl_2.4H_2O$ (> 99% purity), $FeCl_3.6H_2O$ (> 99% purity) and $NaBH_4$ (> 98% purity) were also purchased from Sigma-Aldrich and used as such. 1 µm sized PMMA microspheres were purchased from Sigma-Aldrich (10% by volume). All the glass vials, caps, pipette tips and Millipore water were autoclaved to sterilize the equipment for elimination of any possible contaminants.

Characterization

UV-Vis spectroscopy was carried out by using MINI-D2T deuterium tungsten light source and USB4000 Miniature fiber optic spectrometer from Ocean Optics. Field emission scanning electron microscopy (FESEM) was used to evaluate morphologies of the samples and study them. Images were taken by using ULTRA PLUS and Leo 1530 from Carl Zeiss. TEM images were obtained with a LEO 912ab transmission electron microscope. X-ray diffraction (XRD) patterns were obtained from the samples deposited on a silicon substrate with a native oxide layer using a grazing incidence x-ray diffraction (GIXRD) using a PANalytical X'Pert Pro MRD diffractometer with Cu Kα radiation (λ = 1.54 Å) at an incidence angle of 0.4°. X-ray

photoelectron spectroscopy (XPS) was used to study the oxidation state and compositions of the iron oxide-gold nanoparticle composite. The instrument used for this purpose was Thermo-VG Scientific ESCALab 250 Microprobe equipped with a monochromatic Al K-alpha X-ray source (1486.6 eV). Zeta Sizer Nano ZS90 from Malvern Instruments was used for measuring both zeta potential and size distribution of our samples. Optical microscope DMI 3000 B from Leica equipped with a Hamamatsu CCD was used for optical imaging.

Assembly and Formation of Nano-nets

270 μL of a solution containing both 1 mg/mL $FeCl_2$ and 2.718 mg/mL $FeCl_3$ dissolved in Millipore water was added to a glass vial which contains 4.0 mL of the stock Au nanoparticles. The final solution was put on a shaker for eight hours for assembling of Au nanoparticles. As the 10 nm Au nanoparticles interact with the Fe^{2+} and Fe^{3+} ions and self-assemble into chains, the solution mixture becomes blue in colour. 600 μL of 10 mg/mL $NaBH_4$ was added to the Au-Fe nanoparticle chains to reduce Fe^{2+} and Fe^{3+} ions to Fe^0. The Fe on contact with air is oxidized immediately (within 15 – 30 minutes) to Fe_2O_3. The composite in the vial is now magnetic and the gold chains can now be pulled with the help of a handheld magnet. Magnets are ¾ inch ceramic disks sold by Hillman. 4-8 pieces of magnet stacked on top of each other are used to pull the chains on to the sides of the vial which can be easily removed later.

Bacterial Concentration Determination

Nutrient agar plates were prepared by dissolving 2.8g of nutrient agar in 1 litre of water and autoclaving the solution at 121° C for fifteen minutes. The solution was cooled until it reached 40°-50° C and then poured into petri-dishes. CFUs were determined by plating the solution before and after extraction of the bacteria (or as required) on the Agar plates and after being

incubated overnight at bacteria growing conditions (37° C and no light exposure). The CFU was calculated using the formula: CFU/ml = (no. of colonies x dilution factor) / volume of culture on plate. The microspheres and the microbes were also counted using Brightline haemocytometer made by Hausser Scientific and following the accompanying instructions.

Results and Discussion

The nano-nets are made by mixing Au nanoparticles (10-12 nm in diameter, $5.7x10^{12}$ particles/ml) with Fe^{3+}/Fe^{2+} ions in a pre-determined optimal concentration (0.34 mM of Fe^{2+} and 0.68 mM of Fe^{3+}, details in experimental section). These Au nanoparticles have a zeta potential of ~ -33 mV due to the presence of citrate molecules on their surface.[49] As a result of the interaction between the multivalent cations Fe^{3+} (and Fe^{2+}) and their surface anionic groups the nanoparticles assemble into microns long branched chain like structures.[14,50–53] A typical morphology of these chains can be seen in the TEM image of Figure 2.1a. The higher magnification image of Fig. 2.1b (and its inset) shows that openings of size 80-300 nm are observed between these chains. Also there is ~ 1-2 nm spacing between the adjacent nanoparticles due to the Fe ions. The Fe ions are then reacted to form Fe-oxides (details in experimental section), which transforms these chains into continuous structures similar to nano-nets. The TEM images of 2.2a (and inset) show that the chains are continuous in nature following the transformation. The concentration of cations (Fe^{2+} and Fe^{3+}) in the Au nanoparticle solution is critical for the assembly process. Au nanoparticles in absence of any cations (Fe^{2+} and Fe^{3+}) are isolated from each other due to negative zeta potential, as seen in the TEM image of Fig. 2.2b. If the concentration of the cations (Fe^{2+} and Fe^{3+}) is reduced to half (of the optimal concentration) the scale of the assembly is significantly reduced (TEM image of Fig. 2.3a). Similarly, if the concentration of the cations is doubled the Au nanoparticles agglomerate due to the high ionic strength of the solution as seen in TEM image of Fig. 2.3b.

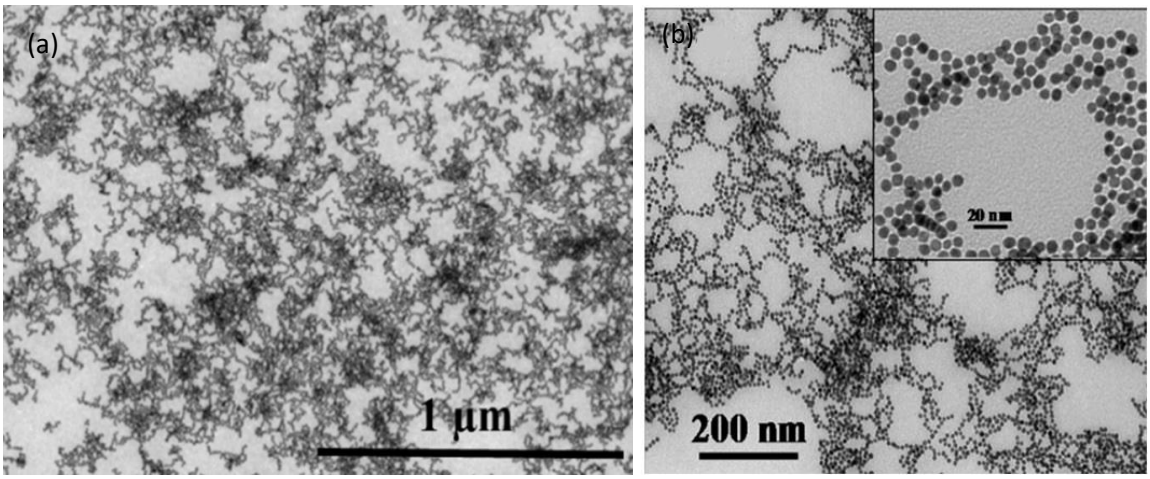

Figure 2.1 (a) TEM images of Au nanoparticles chain like assembly with use of Fe ions in optimal concentration. (b) TEM images of higher magnification images of the chains. (0.34 mM Fe^{2+}, 0.68 mM Fe^{3+} with citrate capped AuNP self-assembled for 8 hours). Scale bar in the inset is 20 nm.

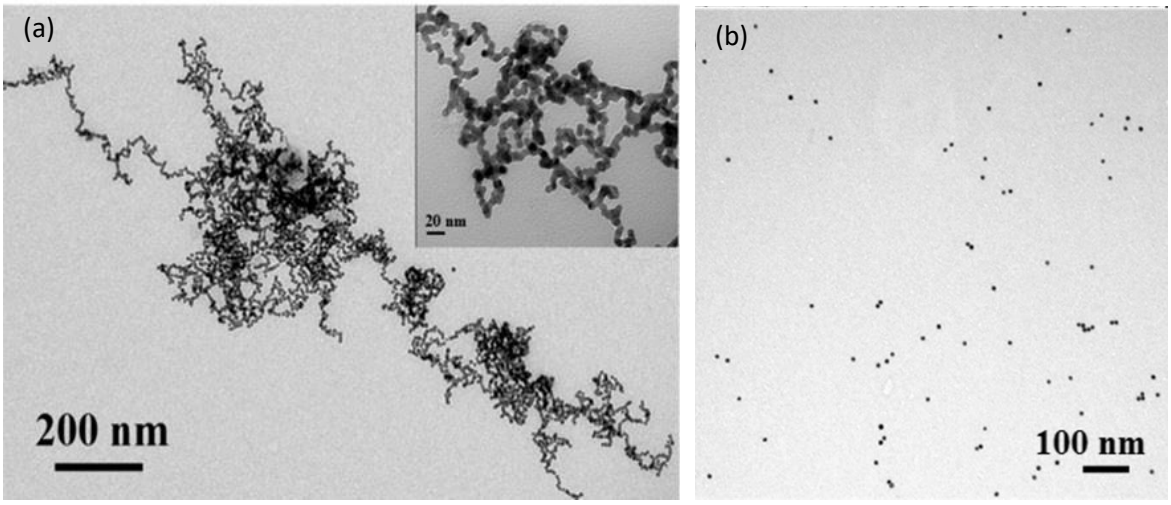

Figure 2.2 (a) TEM images following the transformation of the Fe ions to Fe oxide. (b) TEM image of plain Au nanoparticles in absence of added Fe ions.

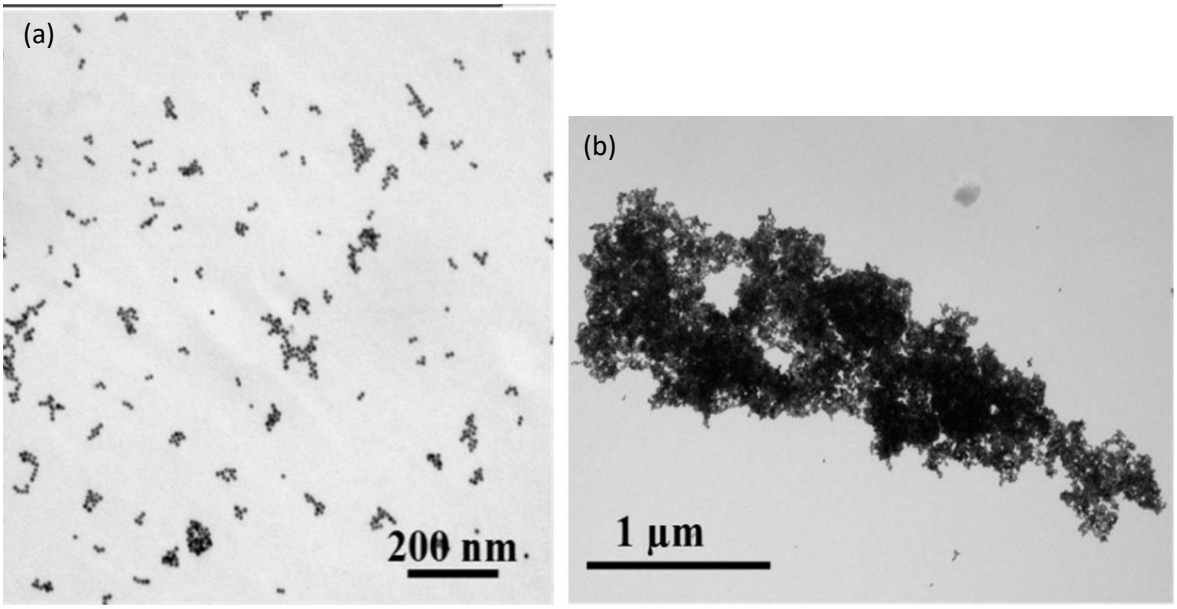

Figure 2.3 (a) TEM image of the Au nanoparticles on adding half of the optimal amount of Fe ions required for assembly (0.34 mM Fe^{2+}, 0.68 mM Fe^{3+} with citrate capped AuNP self-assembled for 8 hours). (b) TEM image of AuNPs on doubling the concentration of the Fe ions. (0.68 mM Fe^{2+}, 1.36 mM Fe^{3+} with citrate capped AuNP self-assembled for 8 hours).

The formation of the Fe oxides in the Au chains is confirmed by a variety of characterization techniques. X-ray diffraction result of Fig. 2.4 shows the peaks corresponding to Au and weak ones corresponding to Fe_2O_3.[54,55] The presence of Fe_3O_4 cannot be ruled out due to close proximity of the peaks between these two Fe-oxides, supporting the conclusion that these are mixed oxides in nature. The XPS results also show the formation of the Fe-oxides (Fig. 2.5a, survey spectra; Fig. 2.5b, Fe 2p; Fig. 2.5c, O 1s; Fig 2.5d, Au 4f). The Fe $2p_{3/2}$ and Fe $2p_{1/2}$ peaks are centred at the binding energies of 711.3 eV and 724.8 eV which are the typical values for Fe^{3+} in Fe_2O_3.[56,57] A satellite peak of the main Fe $2p_{3/2}$ which is located centred at 719.4 eV further indicates the presence of Fe^{3+} species.[57] The O peak centred at 530.2 eV pertains to the lattice oxygen of Fe_2O_3, while the O peak located at 532.5 eV corresponds to the oxygen

defects in the metal oxide matrix and the O in SiO_2.[57–59] The O peak at 532.5 eV is higher in intensity than the first because the XPS measurements were performed on Silicon substrates which contributes to a higher intensity signal. These observations support the conclusion that Fe ions in the chains transform to Fe-oxides and are composed of predominately Fe^{3+} oxides. The reaction of the Fe ions into Fe-oxides also makes these chains magnetic. The optical images of Fig. 2.6 show that on applying a magnetic field using an off the shelf magnet, the chains are completely pulled out and the solution loses colour. The UV-Vis absorption spectra presented in Fig. 2.7 further show these transformations. The plain Au nanoparticles have a typical SPR peak at ~ 525 nm, on assembling into branched chains this peak shifts to ~ 627 nm due to the overlap of the SPR between adjacent nanoparticles as their separation is ~ 1-2nm (Fig. 2.1a&b).[60,61] On reducing the chains to form the nano-nets the spectra shows a broad absorption due to the Fe-oxide nanostructures.[62,63] On pulling out the nets from the solution using a magnet, the UV-Vis shows a flat line attesting to the removal of the Au-Fe nano-nets and their magnetic nature. Both the reduced and unreduced chains have a zeta potential of ~ -30 to -40 mV leading to their stability in water.

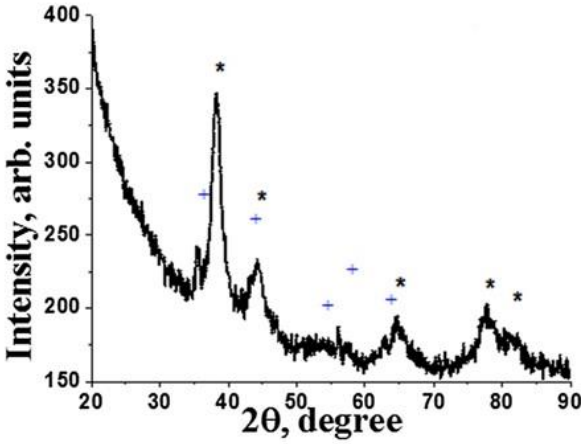

Figure 2.4 The XRD spectra shows peaks corresponding to Au (*) and Fe_2O_3(+)

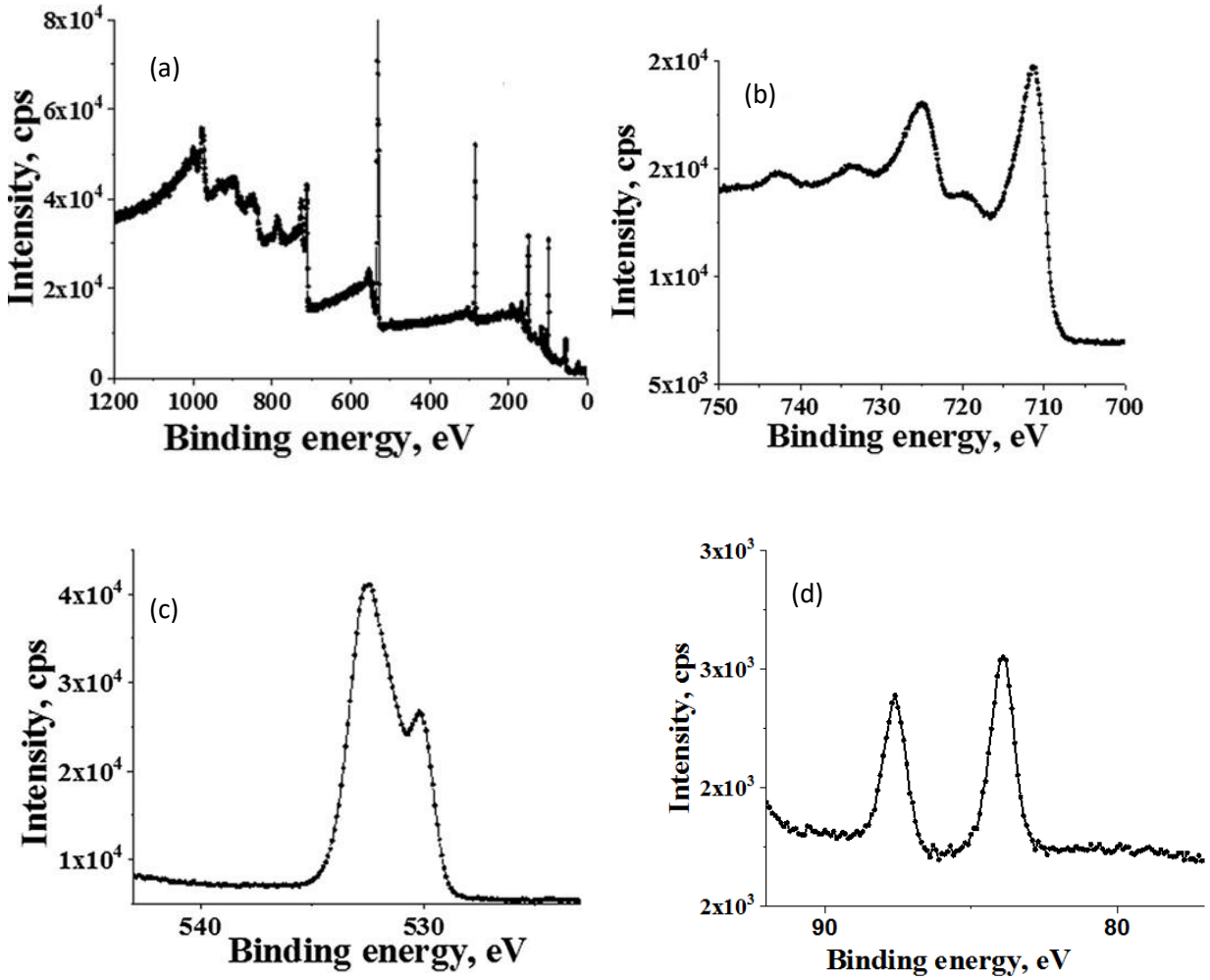

Figure 2.5 (a) The survey spectrum from XPS. (b) The Fe 2p spectrum (c) The O 1s spectrum (d) The Au 4f spectrum.

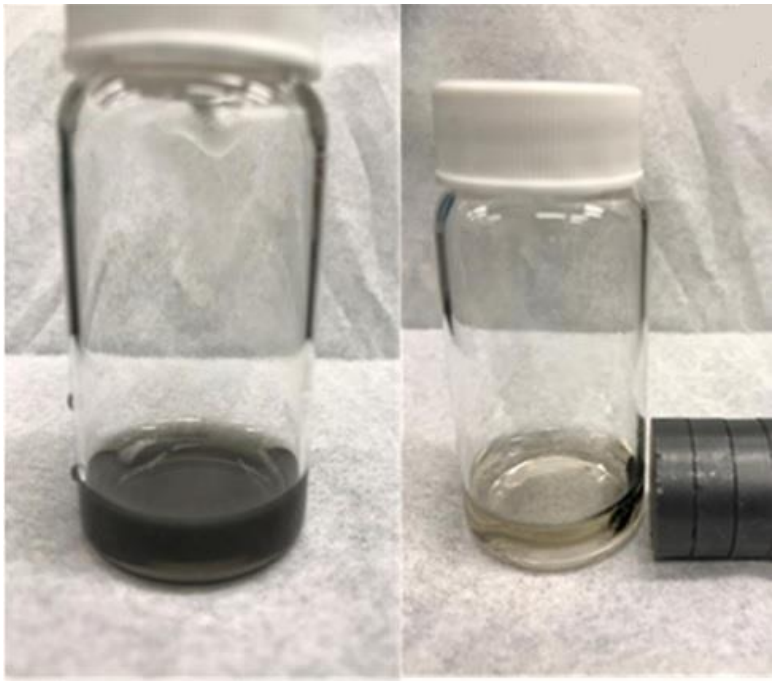

Figure 2.6 The optical image on the left shows the stable colloidal solution of the nano-nets, on right the nano-nets are pulled out of the solution by using an off the shelf magnet.

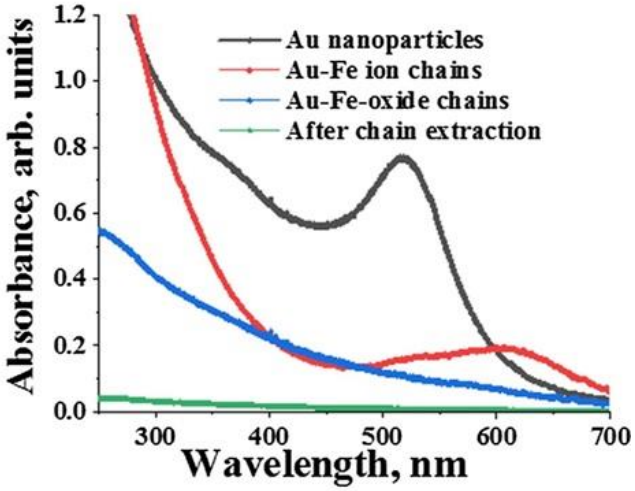

Figure 2.7 The UV–Vis absorption spectra of, colloidal Au nanoparticle solution (grey), their chain like assemblies by use of Fe ions (red), nano-nets on formation of Fe oxides (blue) and following their extraction of the residual solution (green).

The ability of these nano-nets to extract microbes from water is shown by adding them to a solution of the E. coil cells. The microbes are present in concentration of $2.0x10^6$ CFU/ml, and the concentration of Fe added is 0.053 mg/ml (0.95mM). After the addition, a magnet is used to swirl the nano-nets in the solution for 1 min and then held stationary to pull them out. Subsequently using Agar plates the viable microbe concentration in the solution after extraction is determined to be $2.5\ x10^5$ CFU/ml (the average of three replicates). This provides an inactivation ($\log(N/N_0)$; N is the remaining and N_0 is the initial CFU/ml) of -0.9 for the nano-nets. The nano-nets effectively remove more than 87% of the microbes in less than 5 min. This leads to E. coli inactivation efficiency of 0.2 log(inactivation)/(mg/L . h). The removal of the E. coli from the solution is also confirmed by counting the cells using a hemocytometer which provides an E. coli concentration of 2.9×10^5 cells/ml in the residual solution (the average of three replicates). These results show that the nano-nets are effective in physically capturing and removing the E. coli from the solution. The concentration of Fe used here is comparable to that of plain Fe[32,37] and Ag[28,29] nanoparticles used as anti-microbial agents. Further this is achieved in a non deaerated solution within 5 minutes, simplifying the use of nano nets, unlike deaerated solution[32] typically used for achieving high efficiencies with Fe based nanoparticles. The removed nano-nets show a high density of the E. coli cells attached to them as observed in the FESEM images of 2.8a&b. The TEM images of Fig. 2.9a&b show that the Au-Fe nano-nets attach to the surface of the microbes at multiple places (circled in red in Fig. 2.9b and its inset). This multi point interaction over a large area of the microbes allows them to be pulled with the nano-nets on applying a magnetic field. The microbes appear dark in TEM images due to the attachment of these nets which are made of transition metals (2.9a&b). In contrast a plain microbe appears semi-transparent (inset of Fig. 2.9a). On plating these nano-nets with the

extracted microbes on Agar plates the viable CFU were reduced by 80%. This shows that the cytotoxic effect of the Fe oxides in the nano-nets neutralizes the extracted microbes. The magnetic nano-nets hence have a dual action, first due to their high aspect ratio and net like structure they are able to physically capture the microbes with high efficacy from the solution (as seen from the agar plating, hemocytometer counting, and electron microscopy images) and hence act as effective microbial extraction agents. Second, as an added benefit following the extraction due to the close proximity between the microbes and Fe-oxides in the nano-nets their cytotoxic effect leads to neutralization of the captured microbes (as seen from the agar plating results).

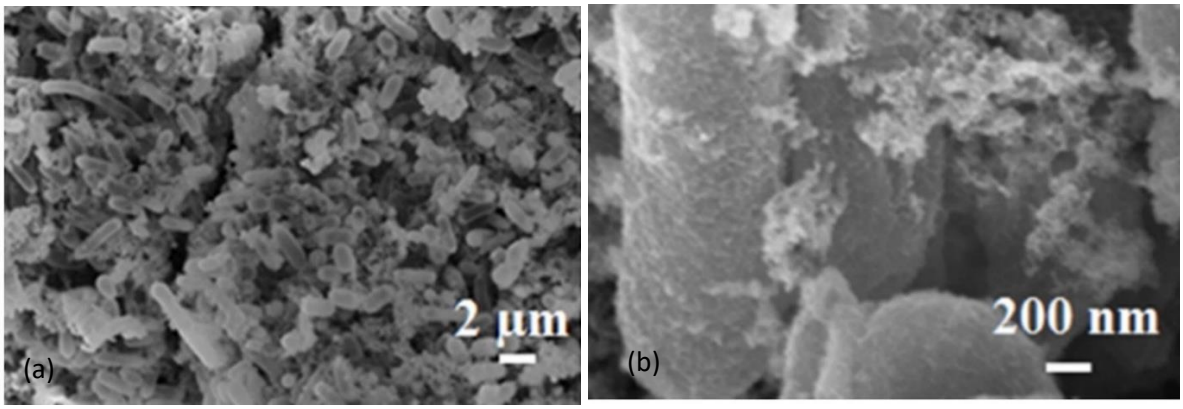

Figure 2.8 (a) The FESEM image of the pulled out nano-nets from *E. coli* contaminated water. (b) A higher resolution FESEM image of the pulled out nano-nets.

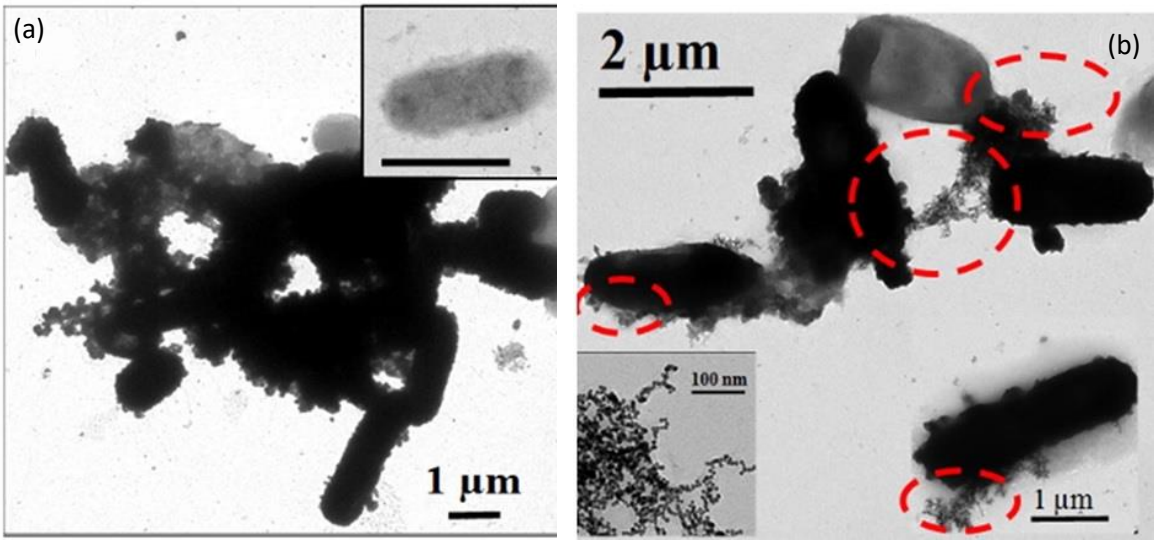

Figure 2.9 (a) TEM image of the pulled out nano-nets and the *E. coli*. The inset is a plain *E. coli* cell. Scale bar in the inset is 2 µm (b) High magnification TEM of the nano-nets and the captured *E. coli* cells. Scale bar in the left inset is 100 nm.

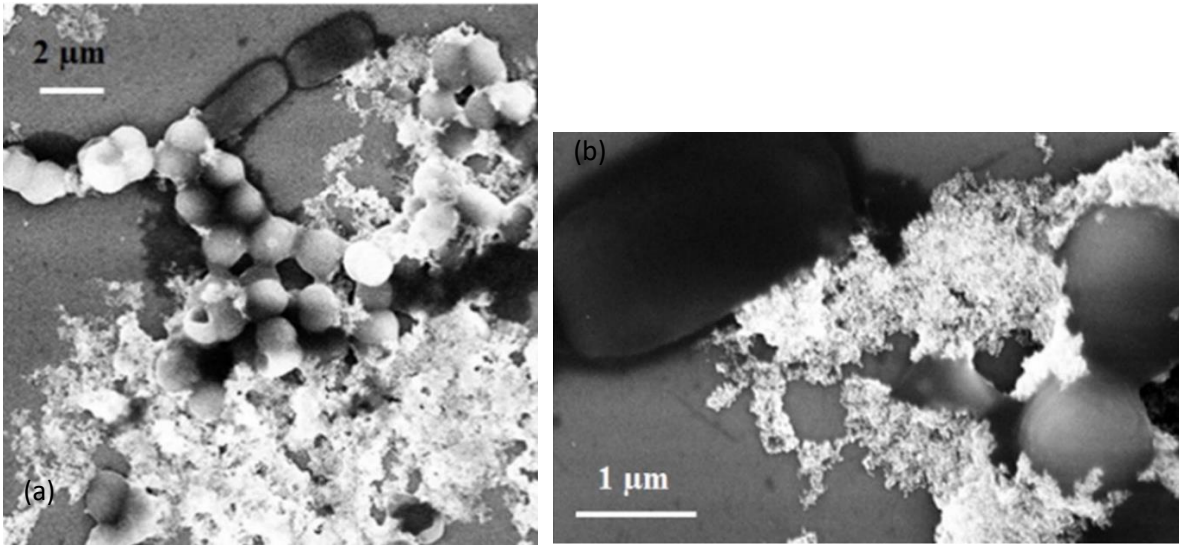

Figure 2.10 (a) FESEM image of nano-nets pulled from a solution of *E. coli* and *S. cerevisiae* (b) High magnification FESEM image of the nano-nets are attached to both the microorganisms.

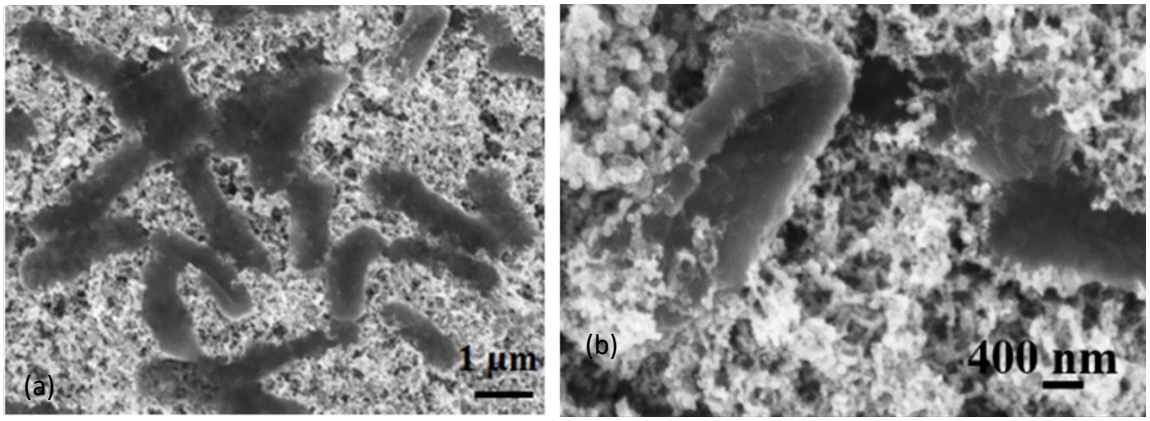

Figure 2.11 (a) FESEM image of the nano-nets and the captured gram positive bacteria *Bacillus subtilis* (b) A high magnification image shows the nano-nets attached to the surface of *Bacillus subtilis*.

A mixture of E. coli (a gram negative prokaryotic microbe) and S. cerevisiae (a eukaryotic microbe) is also subject to successful removal by the Au-Fe nano-nets, as can be seen in the FESEM images of 2.10a&b, where both these microbes can be clearly seen attached to the nano-nets. The nano-nets capture both the microbes with similar effectiveness as determined by their initial ratio in the solution and that in the extracted nano-nets. Both these microbes have a negative zeta potential[64] and hence their interaction with the nets is not based on electrostatic interaction. The ability of the nano-nets to capture a variety of microbes is further confirmed by using them to successfully capture gram positive bacteria Bacillus Subtilis, as seen in the FESEM images of 2.11a&b. The nano-nets can be clearly seen attached to the microbes. Hence the nano-nets can successfully target a variety of microbes and can be used as a generic method for their extraction.

Two set of control experiments are conducted to evaluate the effect of just the Au nanoparticles on the E. coli microbes (each experiment is conducted in triplicate for error analysis). For the first experiment, three identical sets of E. coli contaminated solutions each with a $2.0x10^6$ CFU/ml are prepared. Then to the first solution just plain Au nanoparticles, to the second solution the nano-nets, and in third solution just plain autoclaved water is added (as control). Both the first and second solution have identical Au nanoparticle concentration of 4.56 x 10^{12} particles/ml. The second solution due to the presence of Fe-oxides in the nano-nets also has Fe concentration of 0.95 mM. Following 5-10 min incubation, the nano-nets are extracted from the second solution. The four samples are then plated on Agar for determining the CFUs. The results are shown in Fig. 2.12. The solution with just E. coli and water (control) shows a microbial concentration of 2.1 x 10^6 CFU/ml, the solution with only Au nanoparticles shows a slight reduced microbial concentration of 1.8 x 10^6 CFU/ml. In contrast the extracted nano-nets have a microbial concentration of 4.1 x 10^5 CFU/ml and the solution left following the extraction of the nano-nets has 2.52 x 10^5 CFU/ml. These results show that the Au particles by themselves have limited cytotoxic effects and also cannot be extracted from the solution as they are non-magnetic, while the nano-nets have dual effect, they combine the cytotoxic effects of the Fe-oxides with physical capture of the microbes. To further confirm the limited cytotoxic effect of the Au nanoparticles in contrast to the nano-nets dynamic shake flask method is also used as the second control experiment.[65] The growth curve of Fig. 2.13 clearly show that the nano-nets due to the presence of Fe oxides have cytotoxic effects on the microbes which significantly reduces their CFU count and leads to a lag in their growth, while the Au nanoparticles have a little or no effect in this regard.

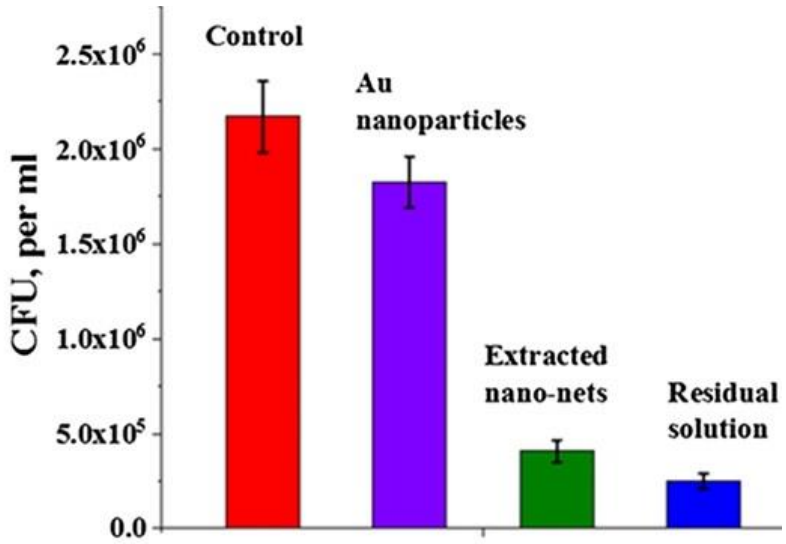

Figure 2.12 The effect on *E. coli* based on CFU count due to exposure to Au nanoparticles and the nano-nets.

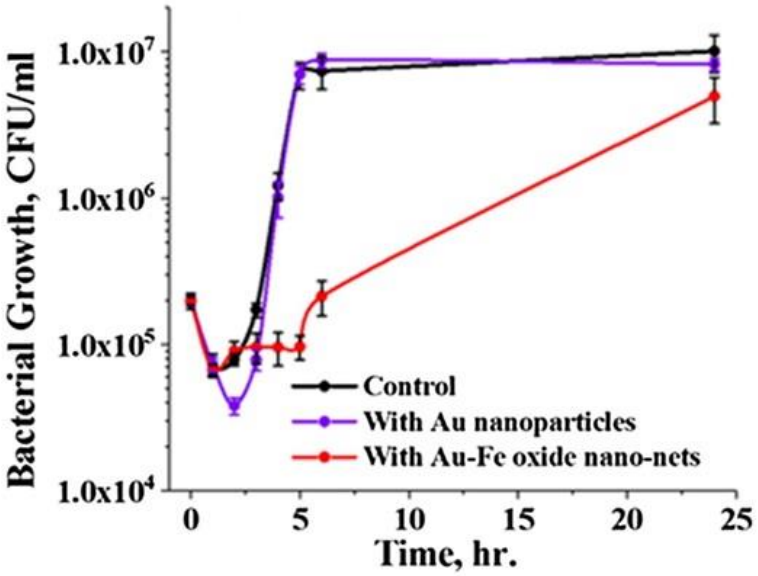

Figure 2.13 Results from the dynamic shake flask method on exposure of the *E. coli* to Au nanoparticle and the nano-nets.

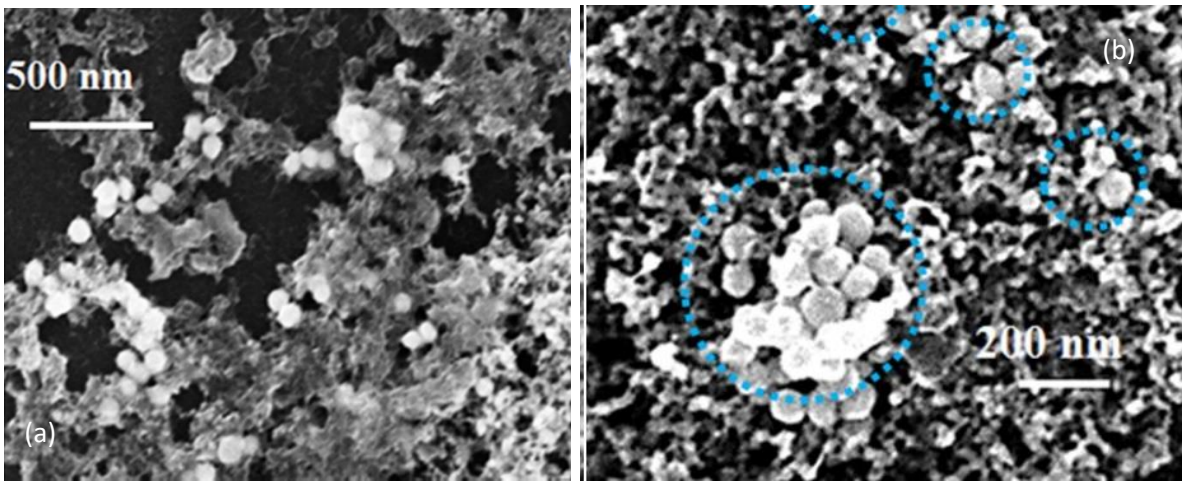

Figure 2.14 (a) FESEM images of the nano-nets pulled from 100 nm Au nanoparticle solution. (b) Higher magnification images of the extracted nano-nets with attached 100 nm Au nanoparticles.

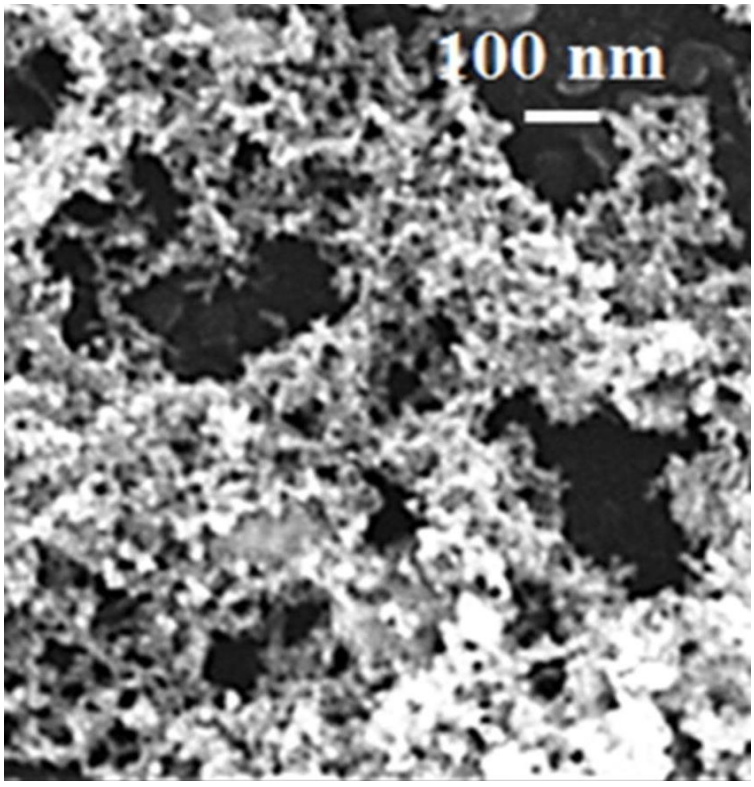

Figure 2.15 FESEM image of the extracted nano-nets from 50 nm Au nanoparticle solution.

The ability of the nano-nets in terms of the size of contaminants that can be captured is characterized by using 100 nm and 50 nm Au nanoparticles. Both these nanoparticles also have a negative zeta potential and hence do not have electrostatic interaction with the nano-nets which also have a negative zeta potential. This is unlike the interaction between the oppositely charged Fe^{2+} and Fe^{3+} cations and the negatively charged Au nanoparticles that leads to the formation of the Au-Fe ion chains. First using a solution of 100 nm Au nanoparticles (concentration of $5.6x10^9$ particles/ml) is mixed with Au-Fe nets, similar to the microbe extraction, after swirling the nano-nets they are extracted using a magnet. The FESEM images (Figure 2.14a&b) show that the nets are successful in capturing the 100 nm Au nanoparticles. This shows that the nano-nets are able to capture 100 nm size particles effectively. Similar process is repeated with 50 nm Au nanoparticles and following the extraction of the nano-nets their FESEM image (Fig. 2.15) shows that hardly any of the nanoparticles are captured and most of them remain in the solution. The nano-nets hence due to their morphology can effectively extract particles of size larger than 100 nm.

The interplay between the capture efficiency of the nano-nets based on, their volume fraction in the solution and the concentration of the target species is characterized by a series of experiments. This is done by adding the nano-nets to a solution of PMMA microspheres that have a size 1 μm and a negative zeta potential (-44 mV), similar to microbes. The PMMA microspheres are used due to their well-defined size and number density in solution. First we conduct the capture of the PMMA microspheres by increasing their concentration in solution while keeping the number of nano-nets constant. Figure 5a shows that the capture efficiency follows a S-shaped curve (inverted) on increasing the microsphere concentration. This is related to the saturation of the collection by the nano-nets as they reach their capacity to interact with

the microspheres. The line is a fit based on power law. A parallel experiment is then performed with E. coli and as seen in Fig. 2.16 (blue curve) a result similar in nature to that of the microspheres is obtained, this attests to the viability of using the microspheres in these experiments. In the second experiment the concentration of the PMMA microspheres is kept constant at 1.15×10^{6} microspheres/ml in the solution and the volume fraction of the nano-nets is varied from $\sim 5 \times 10^{-4}$ to 1×10^{-3} %. The capture efficiency of the nets is shown in Fig. 2.17. We observe a typical S-shaped curve with capture efficiency increasing from 1.6% to 90% with increasing nano-net volume fraction. The line curve in the figure is the fit done using a typical power law. This result is similar in nature to the rise in electrical conductivity of a composite with increasing volume fraction of a conductive filler.[66] We observe from both these analyses that 50% capture is achieved at nano-net volume concentration of 7.8×10^{-4}% and at PMMA microsphere concentration of 3.1×10^{6} particles/ml. There is however an interplay between the two parameters. The limiting number of particles that can be captured is governed by the maximum capacity of the nano-nets as shown in Fig. 2.18. Also the ability to capture the particles is dependent on the volume fraction of the chains that dictates their interaction frequency with the PMMA microspheres, below a critical volume fraction this ability decreases drastically.

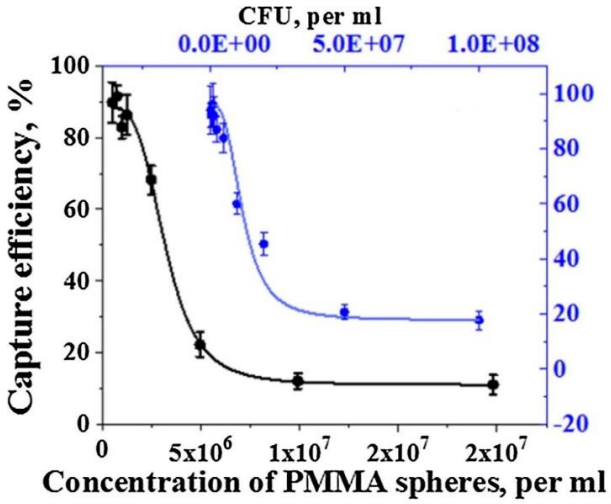

Figure 2.16 The efficiency of the nano-nets for extracting the PMMA microspheres and the microbes is evaluated and fitted using a power law. A constant nano-net concentration on increasing the microsphere and the microbe concentration both show an inverse S-shaped decay in capture efficiency.

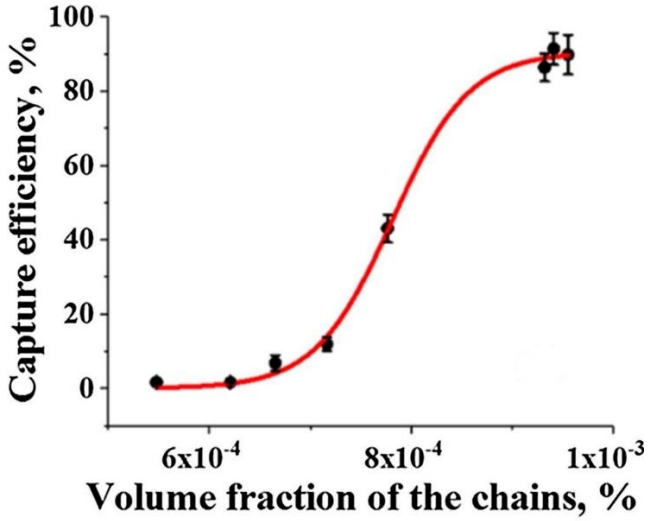

Figure 2.17 For a constant microsphere concentration the extraction efficiency follows an S-shaped curve with the volume fraction of the nano-nets.

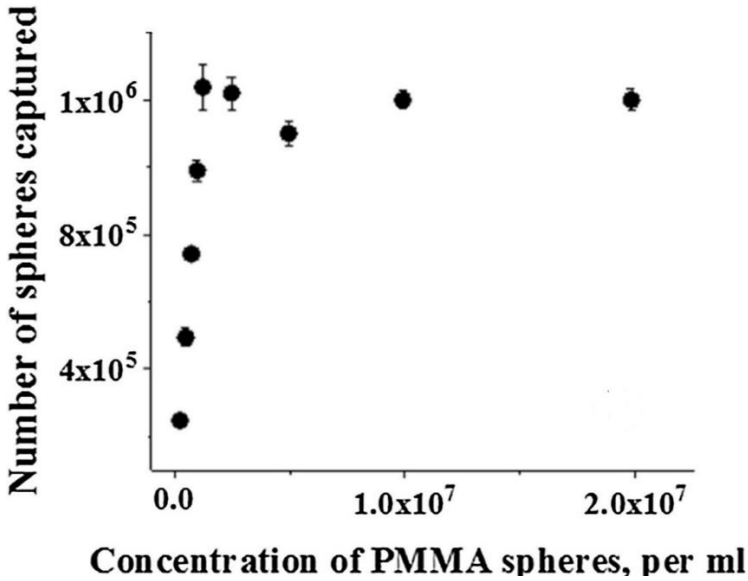

Figure 2.18 On increasing the microsphere numbers we observe that the collection by a fixed number of nano-nets reaches a saturation limit.

Conclusion

The dimensionality of nanomaterials is an important parameter governing their interaction volume with surrounding medium as has been shown for conductive composites.[46] By applying this principle and similar to fishing nets we have designed magnetic nano-nets made of Au and Fe oxides that combine physical interaction with cytotoxic effects for efficient capture of microbes. As a result, due to their diffuse morphology these nano-nets can be used in very small concentrations for capture and extraction of microbes from solution with high efficacy using an off the shelf magnet. This also serves to clean the residual solution of any nano-nets used during the process.[67] The minimum size of particles that can be extracted using these nano-nets is ~100 nm, which is limited by the size of their openings as governed by their self-assembly process. The extraction efficiency of the nano-nets depends on their concentration in the solution as it dictates their interaction volume with the fluid. Since the presented approach uses physical capture of the microbes for their extraction, it will be useful in addressing the challenge of developing microbial resistance to the cytotoxic effects of both anti-biotics and nanomaterials.[22–24,42] Such new strategies are also required due to the increasing range and frequency of water borne tropical diseases related to the changing climate patterns.[68,69] We believe that such strategies based on the ability to make nanomaterials with varying morphology, resulting in physical means to target and neutralize microbes and hence circumventing the need to have a physiological interaction with them, presents a viable option for the future of water purification.

Chapter 3: Enhanced catalytic activity of self-assembled gold nanoparticle cobalt oxide composite chains for oxygen evolution reaction

Introduction

There are concerns regarding climate change and energy security in our world. These two concerns have stimulated the use of renewable energy in the form of solar cells and wind turbines. Due to their intermittent availability, the challenge for these forms of renewable energy sources is the ability to store the energy produced by them for long term use. Batteries and capacitors are able to store energy but are limited by the scale of this requirement and their cost for such large-scale capacity.[70] The splitting of water by electrochemical methods has the potential to act as a source of hydrogen to drive fuel cells. One of the key drawbacks in this process is the lack of efficiency of catalysts for catalysing the electrochemical Oxygen Evolution Reaction (OER). The OER proceeds via a four-electron process.

This reaction step is given by

$$2H_20 \rightarrow 4H^+ + 4e^- + O_2\ E^0 = 1.23V \quad (1)$$

in the acid medium,[71] whereas in basic and neutral medium[72], it is given by the equation

$$4OH^- \rightarrow 2H_2O + 4e^- + O_2\ E^0 = 0.404V(alkaline), 0.817V\ (neutral) \quad (2)$$

In acid medium, the Hydrogen Evolution Reaction (HER) which is the other half reaction of water splitting, is given by the equation

$$4H^+ + 4e^- \rightarrow 4H_2\ E^0 = 0V \quad (3)$$

In alkaline and neutral medium[73], the HER is given by the equation

$$4H_20 + 4e^- \rightarrow 4OH^- + 2H_2\ E^0 = -0.826V(alkaline), -0.413V\ (neutral) \quad (4)$$

The OER is the half-reaction which occurs at the anode and needs to be catalysed by stable and efficient catalysts as it is the limiting step in the electrolysis of water. The HER is quite fast in comparison to OER. Thus, considerable research efforts have been devoted to the development of OER catalysts with the aim of achieving high electrocatalytic activity and stability.[73] Water splitting catalysts can be either electrochemical or photoelectrochemical. We use electrochemical catalysts in our project to catalyse the OER. Noble metal oxides of Ir and Ru are currently the most efficient catalysts.[74] Due to their low availability they are not scalable for commercial production. Recently, earth-abundant transition metal compounds including Cobalt, Iron, Manganese and Nickel oxides and hydroxides have been explored as cheap alternatives for OER.[75,76] However, these compounds have a very low conductivity which limits their electrochemical activity.[76–78] To counter this, we propose a catalyst with high conductivity because of self-assembled gold nanoparticles which cemented by Cobalt oxide. In this work we explore the gold cobalt oxide composite for OER and characterize their catalytic activities with change in composition and structure. Gold being highly electronegative increases the Co^{IV} sites in the CoO_x which is known to catalyse the OER. We also use AuNPs as compared to other works which use bulk gold which is quite expensive.[70] We perform OER in a base since it is known that Co and its oxides dissolve in acid. Our catalysts have an OER overpotential of 430 mV which is better as compared to the Cobalt oxide gold catalyst prepared by Xunyu et al. and our composite exhibits a Tafel slope of 30 mV/dec which is much better than other CoO and Co_3O_4 catalysts.

Materials and methods

Synthesis

Gold nanoparticles were purchased from BBI International. The citrate capped nanoparticles with around 10-12 nm in diameter, $5.7x10^{12}$ particles/ml are stably suspended in water. These Au nanoparticles have a zeta potential of ~ -32 mV due to the citrate capping on their surface, as seen in Fig. 3.1. $CoCl_2$ was purchased from Sigma-Aldrich.

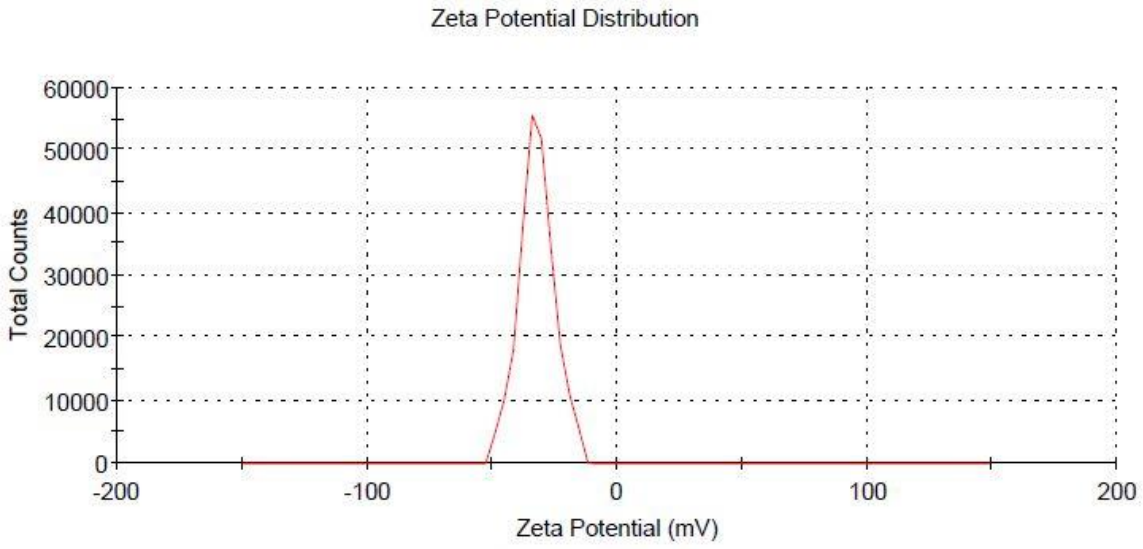

Figure 3.1 Zeta potential of AuNP

All the glass vials, caps, pipette tips and Millipore water were autoclaved to sterilize the equipment for elimination of any possible contaminants. 140 µL of 4 mg/mL $CoCl_2$ was added to a glass vial which contains 2.0 mL of the stock Au nanoparticles. The final solution was put on a vortex mixer for two hours for assembling of Au nanoparticles. As a result of the interaction between the multivalent Co^{2+} ions and these citrate groups the nanoparticles assemble into branched chain like structures. As the 10 nm Au nanoparticles were cross-linked with the Co^{2+}

ions to form larger nanoparticle chains, the solution mixture became blue in color. The color change was caused by the shift of SPR: oscillating electric field of a light ray interact with the free electrons near a colloidal nanoparticle, leading to a concerted oscillation of electron charge resonance with the frequency of visible light. When particle size increases, the wavelength of the SPR absorption shifts to longer wavelengths.

NaOH pellets were purchased from Sigma-Aldrich. 200 µL of 10 mg/mL NaOH was added to the Co-Au nanoparticle chains to convert $CoCl_2$ to $Co(OH)_2$. H_2O_2 was purchased from Sigma-Aldrich. 125 µL of 30% by volume H_2O_2 in water was added to the $Co(OH)_2$-AuNP under constant stirring for ten minutes to oxidise it to CoO_x-AuNP composite. Fig 3.2 shows the process of making the composite from its precursors.

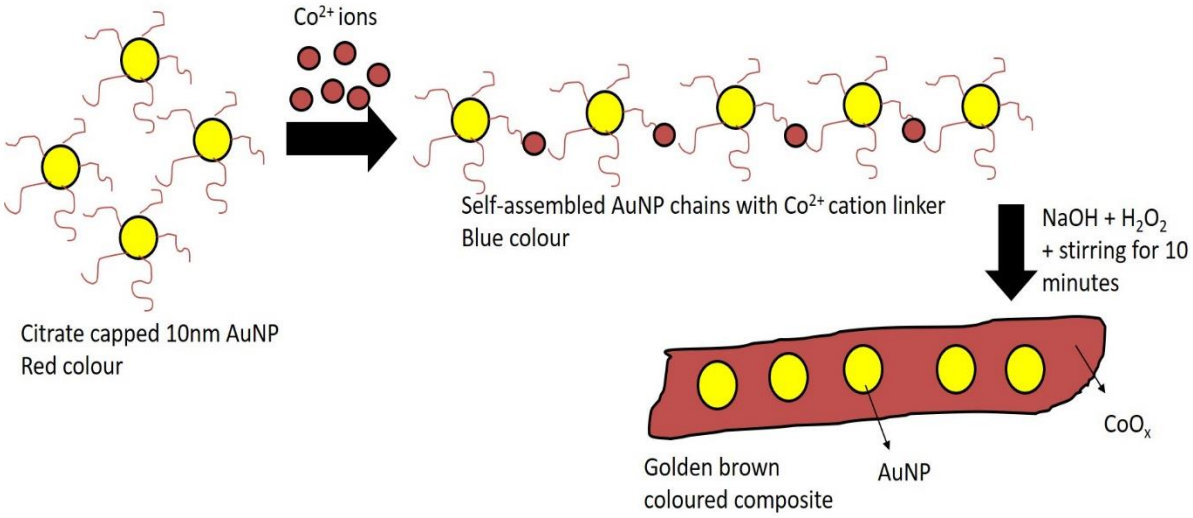

Figure 3.2 Schematic for the step-by-step process of making the CoO-AuNP composite from colloidal gold

Characterization

Ultraviolet-visible spectroscopy was carried out by using MINI-D2T deuterium tungsten light source and USB4000 Miniature fiber optic spectrometer from Ocean Optics.

FESEM was used to evaluate morphologies of the samples and study them. Images were taken by using ULTRA PLUS. TEM images were obtained with a LEO 912ab energy filtered transmission electron microscope (EFTEM).

XPS was used to study the oxidation state and compositions of the CoO-AuNP composite. The instrument used for this purpose was Thermo-VG Scientific ESCALab 250 Microprobe equipped with a monochromatic Al K-alpha X-ray source (1486.6 eV)

Zeta Sizer Nano ZS90 from Malvern Instruments was used for measuring both zeta potential and size distribution of our samples.

Electrochemical measurements were carried out using a CompactStat electrochemical interface & impedance analyzer at room temperature. A standard three-electrode set up was used for all experiments. The setup is shown in Fig 3.3. The measurements are reported with Ag/AgCl (sat KCl) as the reference electrode and platinum wire is used as the counter electrode. A 3 mm diameter glassy carbon electrode (GCE) was used for depositing the catalyst solutions. The GCE was polished using 0.05 μm alumina powder before each measurement. We perform electrochemical measurements using a three-electrode system in 1M KOH as the electrolyte. Alkaline medium is chosen since Co-oxides are known to be stable in this pH. Since Pt is one of the best catalysts for the HER, we use it as the counter electrode. The electrochemical

measurements were performed with constant stirring of the electrolyte at 400 rpm to prevent mass transfer effects.

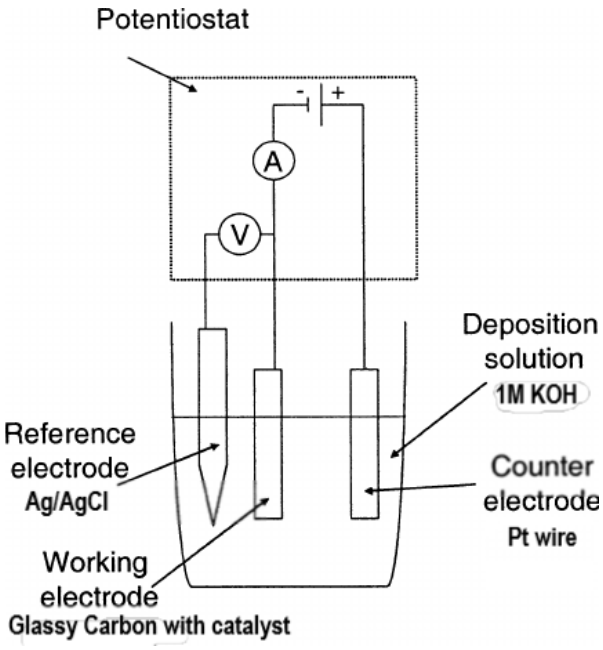

Figure 3.3 The electrochemical setup to test the catalytic performance of our catalyst

Results and discussion

The typical morphology of the chains is characterized through TEM. Fig. 3.4a,b&c. shows the high resolution TEM images of the branched chain like structures with ~1-2 nm spacing between adjacent Au nanoparticles due to the presence of Co^{2+} ions. Following the oxidation of the Co^{2+} ions, the nanoparticles form continuous chains which is shown in Fig. 3.5a,b&c.

The UV-Vis absorption spectra presented in Fig. 3.6 further characterizes the catalyst. The 10-12 nm Au nanoparticles have a typical SPR peak at ~ 525 nm, on assembling into branched chains this peak shifts to ~ 627 nm due to the over lap of the SPR between adjacent nanoparticles as their separation is 1-2nm (Fig TEM). On oxidising the chains to form the electro-catalyst the spectra shows a peak at ~ 390 nm due to the formation of Co-oxide nanostructures.[79]

XPS plots shows the survey spectrum in Fig 3.7 and the presence of Au, Co, O in high resolution spectra as seen in Fig. 3.8a,b&c. The cobalt is in 2+ and 3+ states with the major state as 2+. The $2p_{3/2}$ binding energy of the Co in CoO is around 780 eV and for $2p_{1/2}$ it is around 796 eV.[80] Additionally, there are two satellite peaks corresponding at 786.7 eV and 802.5 eV which agree with literature values of CoO.[80] The presence of Co_3O_4 which has its major peaks $2p_{3/2}$ at 780 eV and $2p_{1/2}$ at 796 eV cannot be ruled out.[81] The O 1s peak is at 529.4 eV which corresponds to the lattice oxygen of the cobalt oxide. The other peak at ~ 532 eV corresponds the oxygen bound to the SiO_2.[80] Since the sample is prepared on a silicon substrate, this peak is observed.

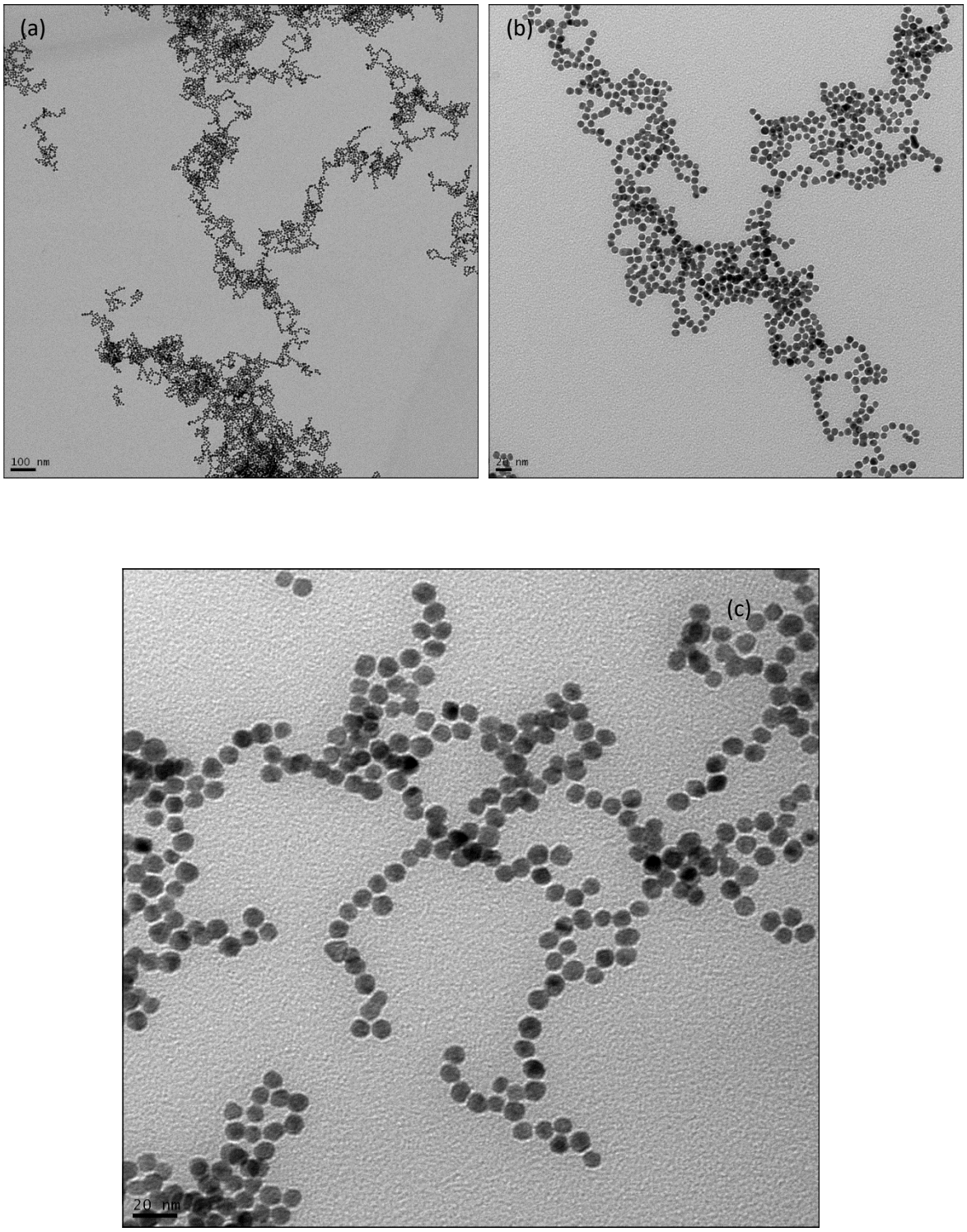

Figure 3.4 (a) TEM image of the AuNP chains self-assembled with the help of Co^{2+} linkers (b),(c) Higher magnification TEM images of the chains. (1.26 mM $Co^{2+}$with citrate capped AuNP self-assembled for 2 hours).

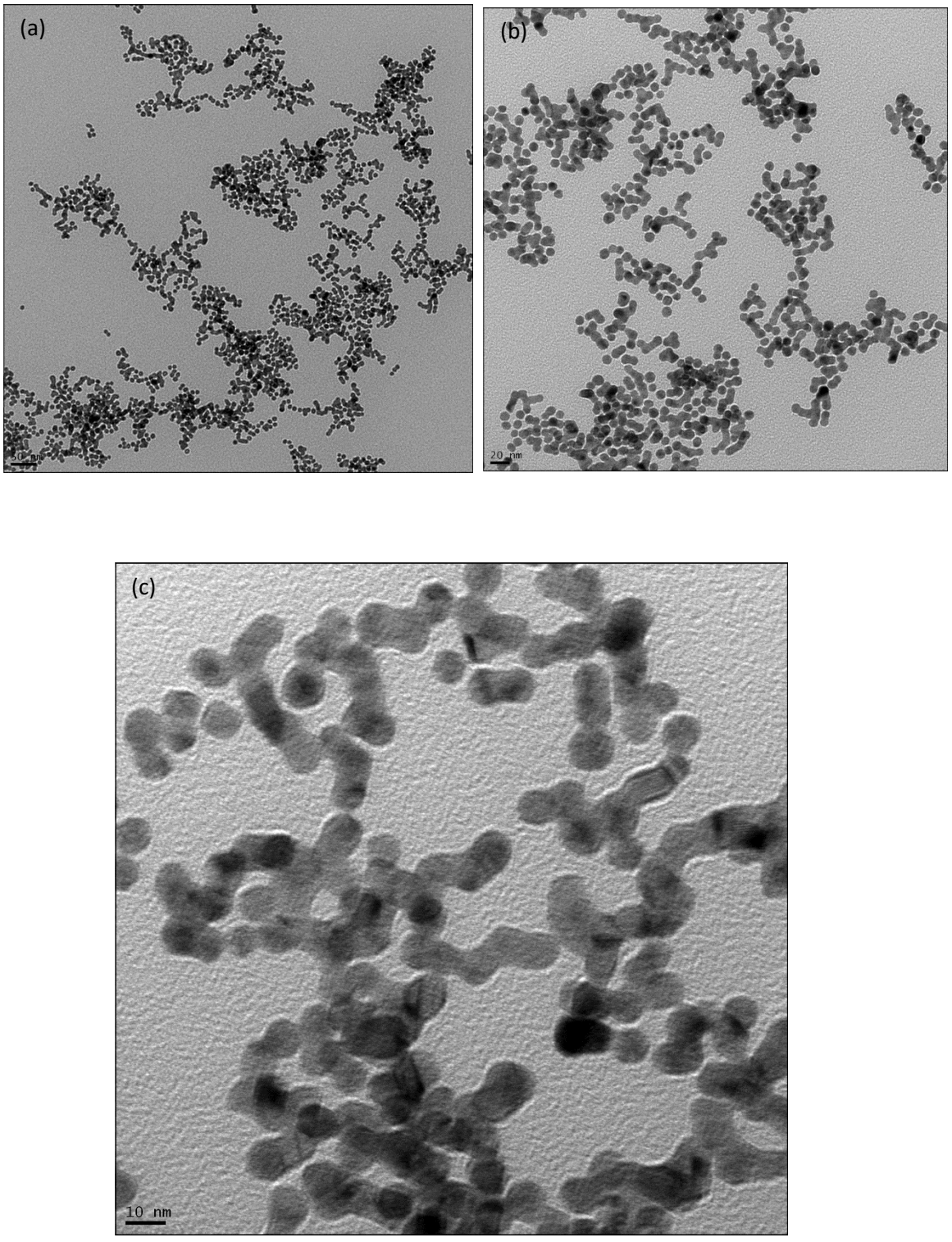

Figure 3.5 (a) TEM image of the AuNP chains with the Co oxidised to its oxides (b),(c) Higher magnification TEM images of the chains.

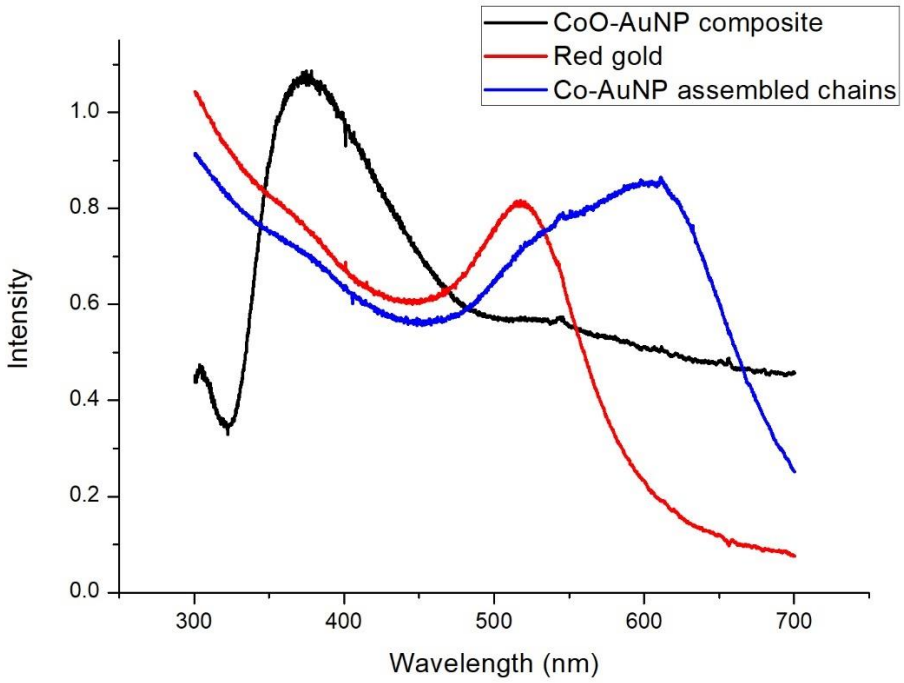

Figure 3.6 The UV–Vis absorption spectra of colloidal AuNP solution (red), their chain like assemblies by use of Co ions (blue) and CoO-AuNP nanocomposite on formation of Co oxides (black).

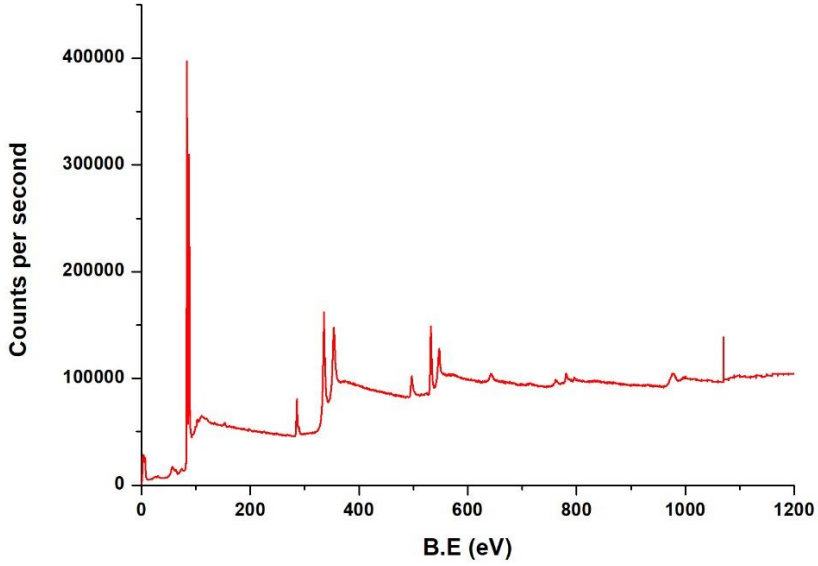

Figure 3.7 The survey spectrum from XPS of the CoO-AuNP composite

(a)

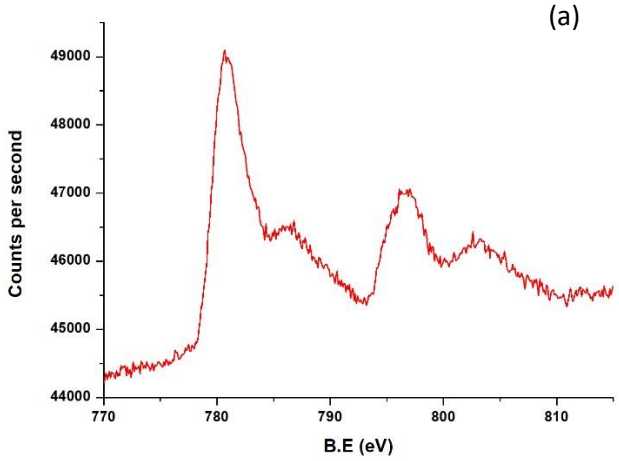

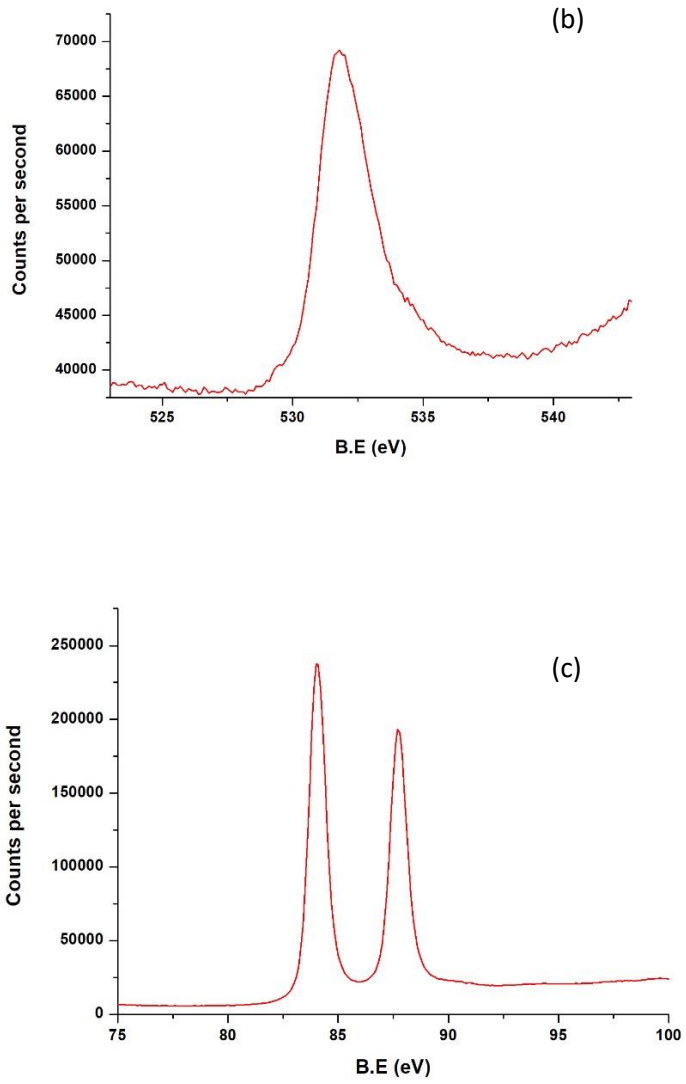

Figure 3.8 High resolution XPS spectra of (a) Co 2p, (b) O 1s, (c) Au 4f.

To test the electrical conductivity of our catalyst, we deposited the catalyst in between gold pads using dielectrophoretic forces. The deposition is conducted between two micrometer-scale electrodes separated by a micrometer-scale gap, immersed in an aqueous medium containing the CoO-AuNP composite. The result is the formation of thread like conduction pathways between the gold pads as shown in the FESEM images in Fig 3.9. The electrical conductivity by measuring the current vs voltage characteristics with the help of a probe station.

The material showed linear ohmic behaviour in the range of 0-1.5 V as shown in the I-V curve in Fig 3.10 with a conductivity of roughly $0.5*10^{2}$ S/cm to $1*10^{2}$ S/cm (considering length of cylindrical chain is 1 µm and cross-section radius is ~ 100 nm) as compared to bulk CoO whose conductivity is $4.35*10^{-3}$ S/cm to $1.6*10^{-2}$ S/cm. More detailed analysis is required to ascertain the true conductivity values of the CoO-AuNP composite where morphology changes during the device fabrication process are minimized.

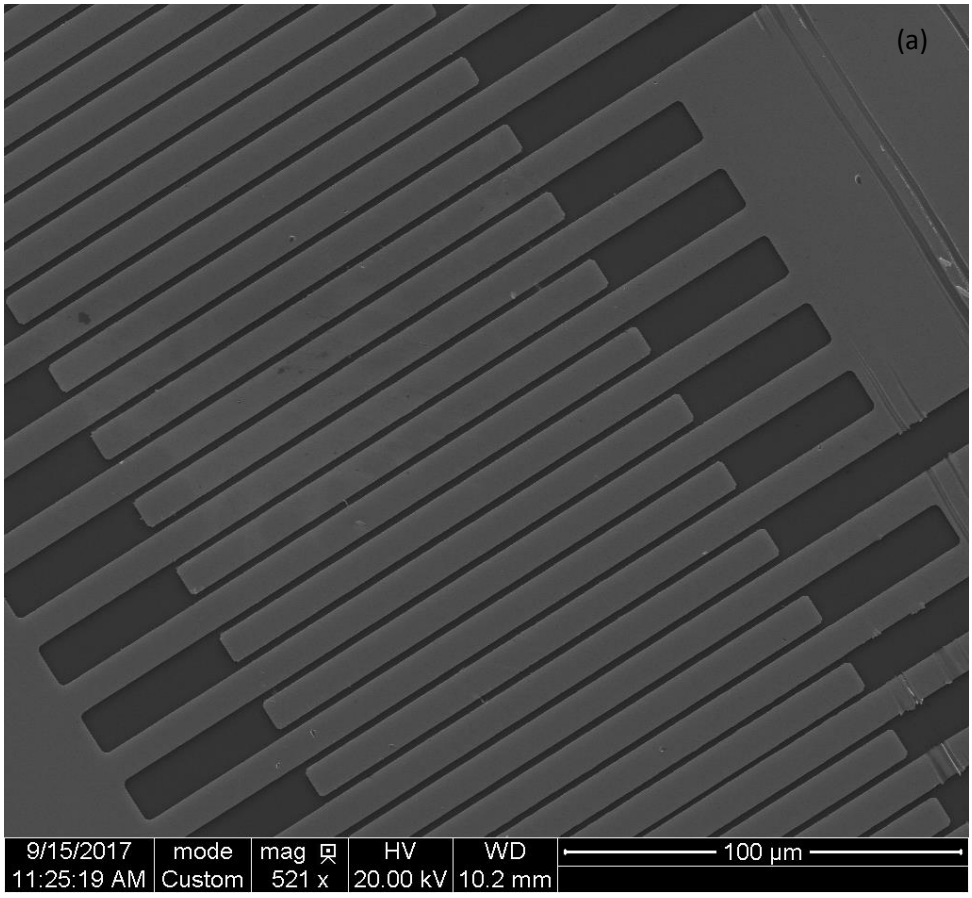

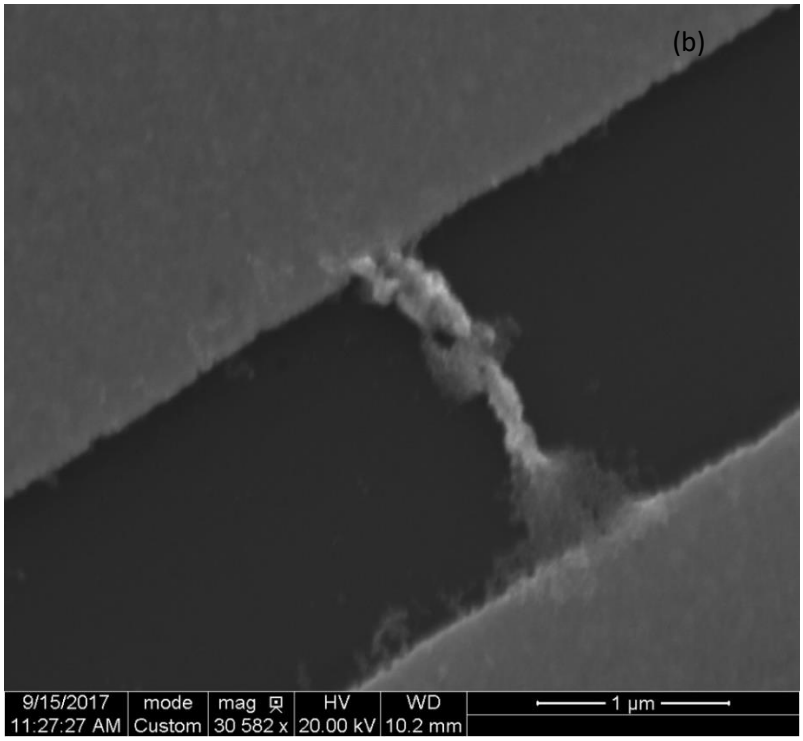

Figure 3.9 (a) FESEM image of the silicon chip with gold pads after depositing the CoO-AuNP chains by DEP. (b), (c) high resolution images of the the silicon chip with gold pads after depositing the CoO-AuNP chains by DEP.

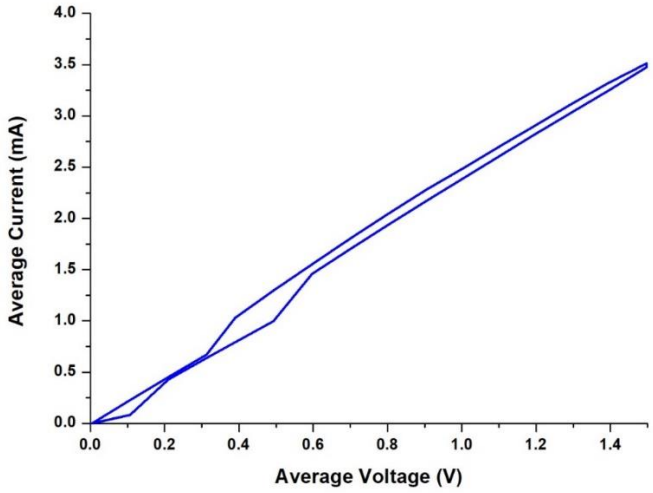

Figure 3.10 Current vs voltage characteristics of the CoO-AuNP composite deposited on the silicon chip with gold pads using DEP.

To evaluate the catalytic activity of the CoO-AuNP composite in the OER of electrochemical water splitting, linear sweep voltammograms (LSV) were recorded at a scan rate of 50 mV/s using CoO-AuNP loaded glassy carbon in 1M KOH solution (details in experimental section). Voltages were recorded using Ag/AgCl (saturated) reference electrode. The TEM images in Fig 3.11a&b. and Fig 3.12a&b. also show an increase in the CoO-AuNP chain length with increase in the time for self-assembly. The UV-Vis spectra in Fig 3.13 also show that the peak wavelengths of absorption redshifts as the assembly time increases. Fig 3.14 shows the LSVs obtained with the CoO-AuNP composite as the time of self-assembly of the gold-nanoparticle chains changes from 10 minutes (partial self-assembly) to 2 hours (completely self-assembled without agglomeration). Also shown are the control experiments with individual AuNP, CoO in water and CoO with individual AuNP mixed together. The completely self-assembled CoO-AuNP composite shows the highest OER catalytic activity with a low onset potential of 0.6 V (vs Ag/AgCl) and an overpotential of 430 mV to obtain a 10 mA cm^{-2} current

density. The overpotential is better by 10 mV as compared to the catalyst prepared by Xunyu et al.[82] The catalytic activity increases with increase in the self-assembly time. Fig 3.15. shows the Tafel plots derived from figure for the fully assembled CoO-AuNP in OER. The composite exhibits a Tafel slope of 30 mV/dec which is less than other CoO and Co_3O_4 catalysts.[70,82]

The turnover frequency was calculated for the CoO-AuNP catalyst by assuming that all the cobalt sites are involved in OER. The turnover frequency (TOF) was calculated from the anodic current density which was obtained from figure. As shown in the table below, at an overpotential of 400 mV, the TOF for our AuNP/CoO chains is 0.07 s^{-1} which is more than the one obtained by Xunyu et al.[82] ($4.8*10^{-2}$ s^{-1}) and that reported by Yang et al.[83] ($4.55*10^{-3}$ s^{-1}). The current density obtained from the AuNP-CoO chains is similar to the current density obtained from the 0.4 ML Co_3O_4 on Au at 351 mV overpotential although the TOF is lesser for our catalyst ($1.2*10^{-2}$ s^{-1}) as compared to 0.4 monolayers (ML) Co_3O_4 on Au (1.81 s^{-1}), which is expected since the amount of CoO catalyst used is more in our case as compared to 0.4 monolayers of Co_3O_4.

Catalyst	Overpotential (mV)	Current density (mA cm^{-2})	TOF (s^{-1})
0.4 ML Co_3O_4 on Au	351	0.8	1.81
AuNP-CoO chains	351	0.74	$1.2*10^{-2}$
mCo_3O_4	400	2.5	$4.55*10^{-3}$
2.5% Au/ mCo_3O_4	400	6	$4.8*10^{-2}$
AuNP-CoO chains	400	4.2	$7*10^{-2}$

Table 3.1 Turnover frequencies comparison table[70,82,83]

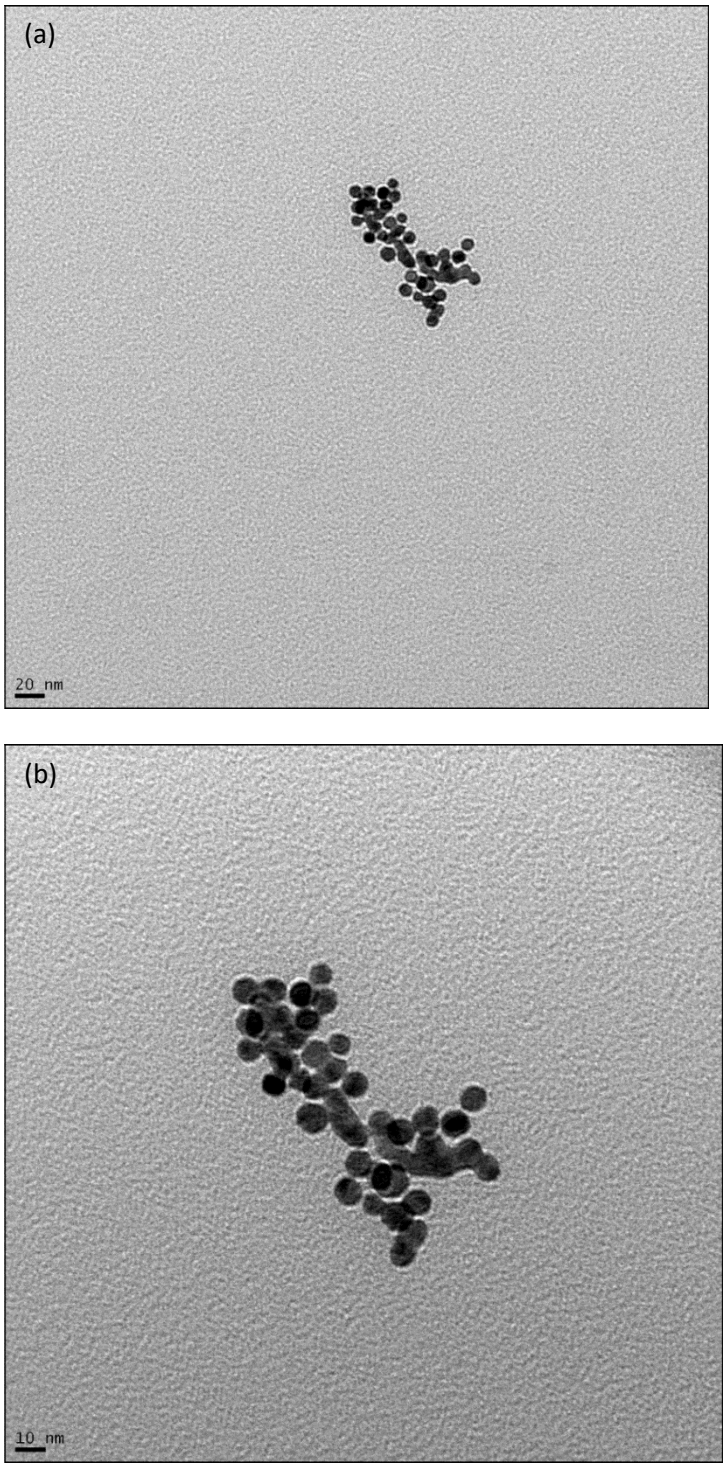

Figure 3.11 (a) TEM image showing the AuNP chains after self-assembling using Co^{2+} linker (1.26mM) for 10 minutes. (b) High resolution TEM image showing the AuNP chains after self-assembling using Co^{2+} linker (1.26mM) for 10 minutes.

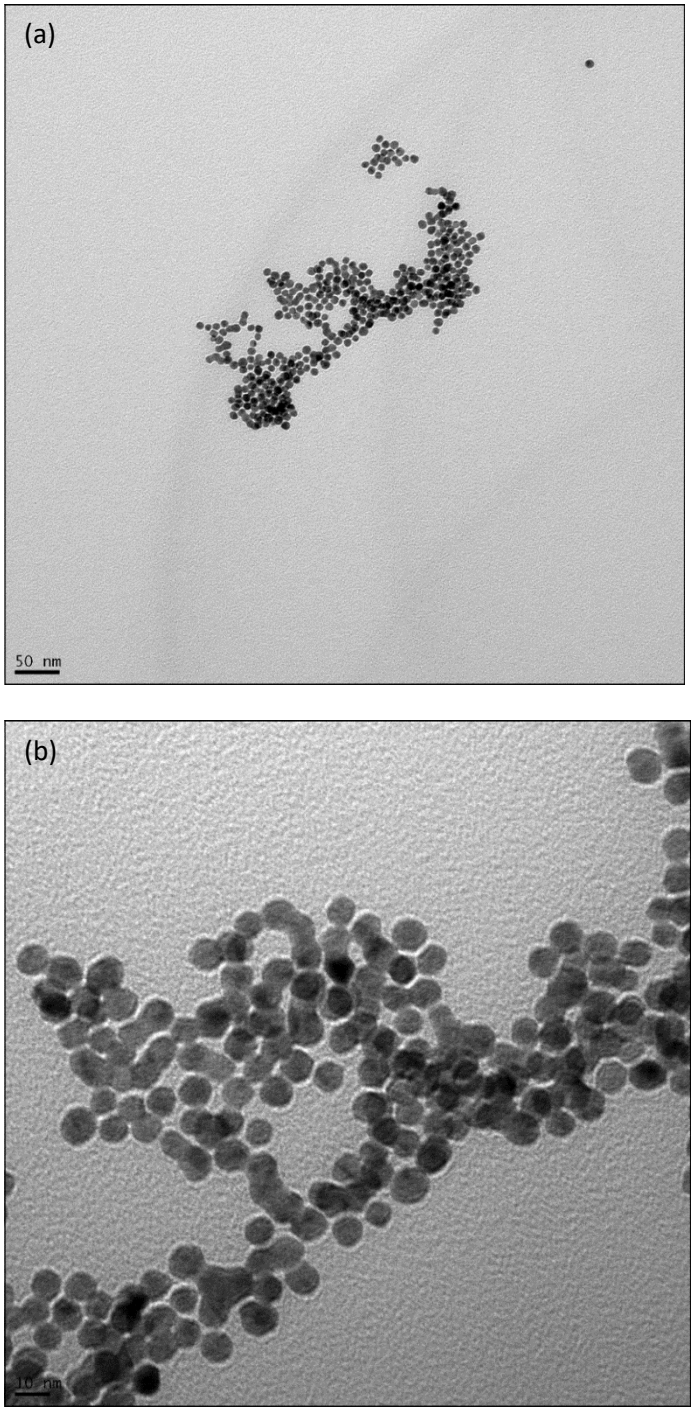

Figure 3.12 (a) TEM image showing the AuNP chains after self-assembling using Co^{2+} linker (1.26mM) for 40 minutes. (b) High resolution TEM image showing the AuNP chains after self-assembling using Co^{2+} linker (1.26mM) for 40 minutes.

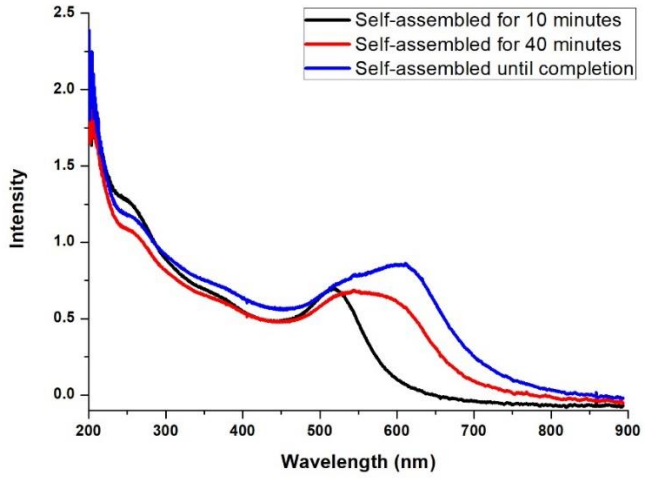

Figure 3.13 The UV–Vis absorption spectra of self-assembled AuNP chains 10 minutes after adding the Co^{2+} linker ion (black), 40 minutes after adding the linker (red) and after complete self-assembly (blue).

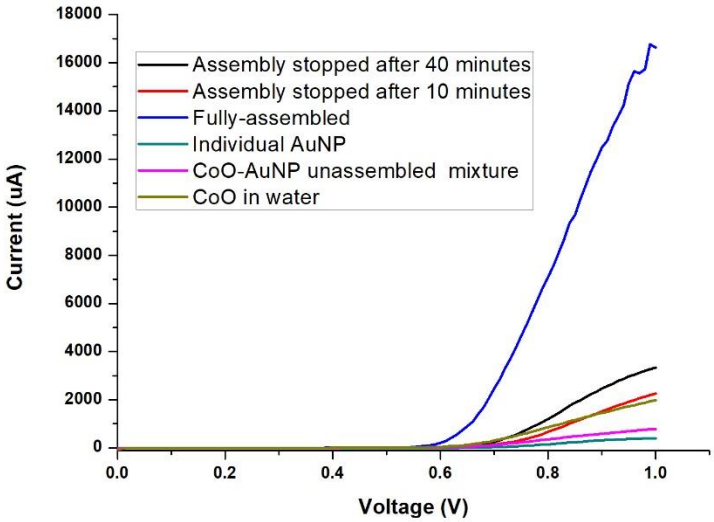

Figure 3.14 LSV curves for individual AuNP (green), self-assembled CoO-AuNP chains assembled for 10 minutes (red), assembled for 40 minutes (black), completely self-assembled

(blue), with controls performed on CoO in water (brown) and a mixture of CoO and individual AuNP (pink).

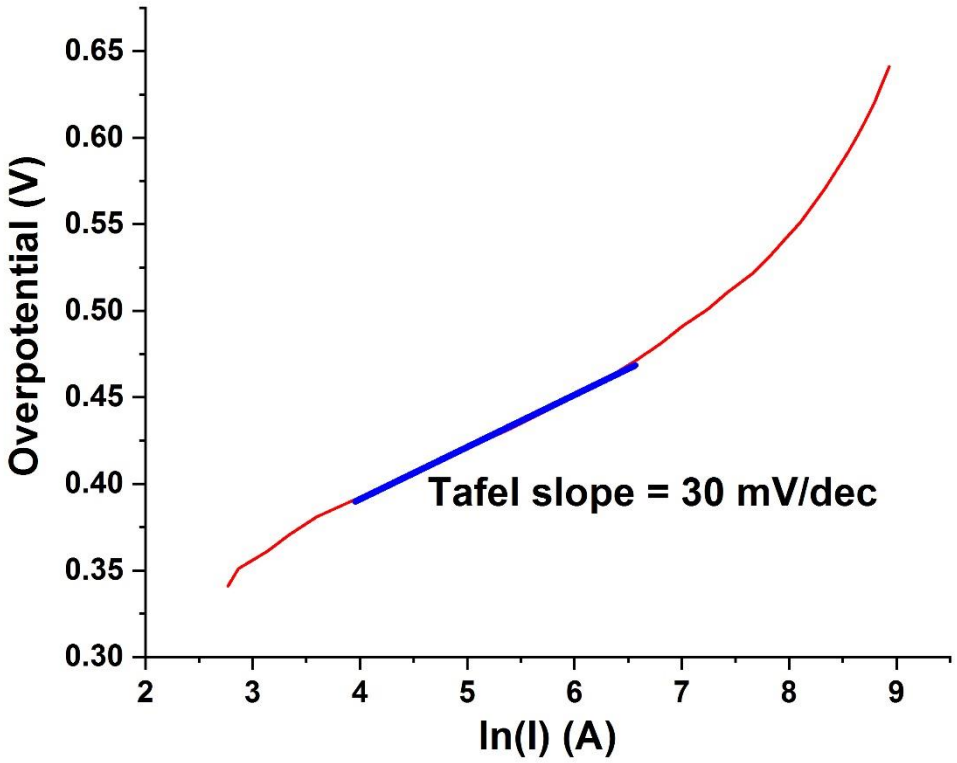

Figure 3.15 Tafel slope of the CoO-AuNP catalyst after complete self-assembly

Another challenge of the cobalt based catalysts is their stability over time. Many of the previous works have not studied this in detail though it is important. Stability measurements were performed on some of our electrodes for 12 hours by measuring the chrono-amperometric response as in Fig 3.16. The fully self-assembled CoO-AuNP catalyst shows that the current of the water splitting reaction reduces slowly and is then maintained at a steady state value for a long time. The current reduces to one third of its initial value in three hours and then remained constant for the remaining time. A similar analysis was done by Alexis Bell group[70] which shows

a similar behaviour for CoO_x deposited on gold electrodes where the current reduces to approximately one third of its initial value in three hours and then remains constant. The similar stability tests were conducted for partially self-assembled CoO-AuNP catalysts. These tests showed that the final steady state current values increased with increasing the time of assembly and were best for the fully assembled catalyst. Control experiment with just CoO in water was performed and it showed a lower steady state current value as compared to self-assembled CoO-AuNP catalysts which shows the importance of AuNP in enhancing the catalysis.

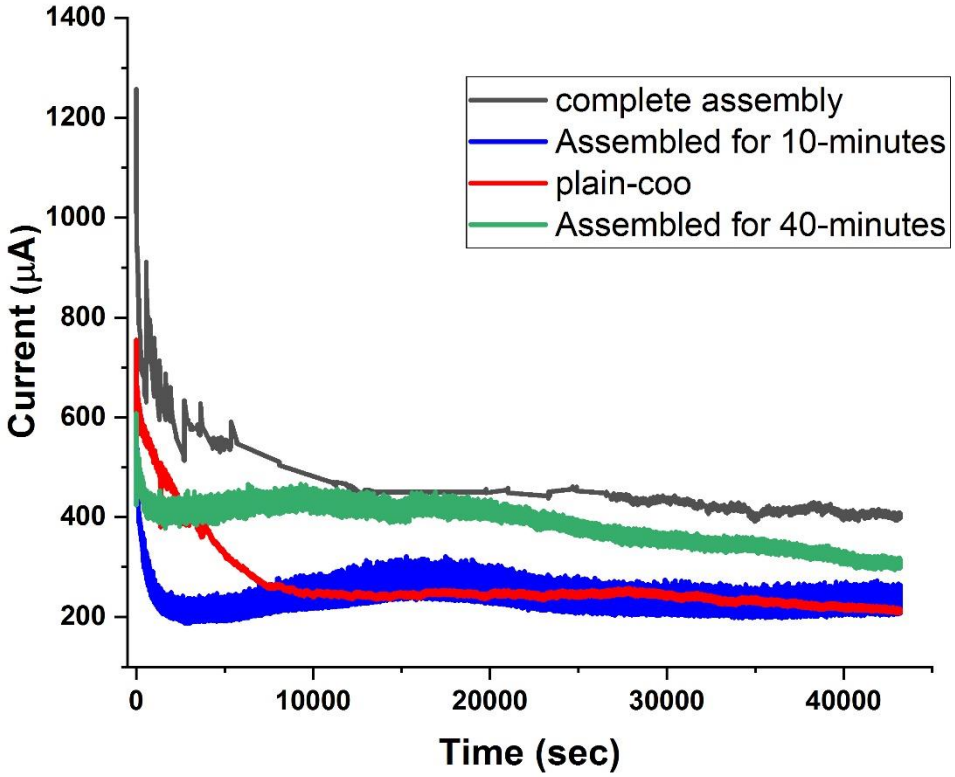

Figure 3.16 Stability curves for plain CoO in water (red), self-assembled CoO-AuNP chains assembled for 10 minutes (blue), assembled for 40 minutes (green) and completely self-assembled (grey).

Conclusion

We researched the catalytic properties of self-assembled Au cobalt oxide chains for the Oxygen Evolution Reaction which is a half reaction of water splitting. Micron sized branched 3-D networks of AuNP were formed with cobalt oxide linkers. The self-assembled structures helped to effectively disperse the catalyst and provided an easy fabrication process for our catalyst at room temperature as compared to other groups who have used methods like atomic layer deposition or high temperature synthesis methods to fabricating their catalysts. The gold template enhanced the conductivity of our cobalt oxide catalyst due to the formation of conductive gold chains. In addition, our catalyst exhibited low overpotential, high TOF and a very low Tafel slope as compared to many previous works. Our experiments were done in a stirred system hence there are no mass transfer effects and hence Tafel slope could be calculated. Tafel slope tells us how much the overpotential must be increased to increase the reaction rate by 10 times. Our catalyst shows low Tafel slope which implies that the reaction rate can be increased by spending lesser energy. Stability studies on our catalyst shows that it is quite stable even after 12 hours of the water splitting reaction.

Final conclusions and future work

The self-assembly of AuNP has been studied and its application to water purification and oxygen evolution reaction of water splitting were investigated. Two nanocomposites were developed: First, iron oxides with AuNP and the second, cobalt oxides with AuNP. In case of the iron oxide-AuNP composite the branched chain like structure acts like nano-nets which in turn help to capture objects which are more than 100 nm in diameter. They can be later separated and removed from solution with the help of a handheld magnet due to the magnetic nature of the chains. The cobalt oxide-AuNP composite also has branched chain like structure. Here the chain like structure helps to disperse the catalyst and enhances conductivity. This structure facilitates dual or triple catalyst systems by forming AuNP chains cemented by other compounds like CoO_x. The method of making this catalyst is very easy compared to other catalysts. Also the composite shows good catalytic properties for the water splitting reaction.

The property of self-assembly of citrate capped AuNP is quite useful and can be applied to future applications like photo and electrocatalysis, making conductive inks, sensors for chemicals and bio-molecules, etc. The cost of the magnetic nanonets can be reduced by replacing gold by other polymers. Other transition metal oxides with AuNP composites must be tested as catalysts for OER. Further rotating disk voltammetry studies can be performed on our catalysts.

References

(1) Li, J. J.; Lo, S. L.; Ng, C. T.; Gurung, R. L.; Hartono, D.; Hande, M. P.; Ong, C. N.; Bay, B. H.; Yung, L. Y. L. Genomic Instability of Gold Nanoparticle Treated Human Lung Fibroblast Cells. *Biomaterials* **2011**, *32* (23), 5515–5523.

(2) Fendler, J. H.; Meldrum, F. C. The Colloid Chemical Approach to Nanostructured Materials. *Adv. Mater.* **1995**, *7* (7), 607–632.

(3) Belloni, J. Metal Nanocolloids. *Curr. Opin. Colloid Interface Sci.* **1996**, *1* (2), 184–196.

(4) Schmid, G. Large Clusters and Colloids. Metals in the Embryonic State. *Chem. Rev.* **1992**, *92* (8), 1709–1727.

(5) Matijević, E. Controlled Colloid Formation. *Curr. Opin. Colloid Interface Sci.* **1996**, *1* (2), 176–183.

(6) Henglein, A. Physicochemical Properties of Small Metal Particles in Solution: "Microelectrode" Reactions, Chemisorption, Composite Metal Particles, and the Atom-to-Metal Transition. *J. Phys. Chem.* **1993**, *97* (21), 5457–5471.

(7) Njoki, P. N.; Lim, I.-I. S.; Mott, D.; Park, H.-Y.; Khan, B.; Mishra, S.; Sujakumar, R.; Luo, J.; Zhong, C.-J. Size Correlation of Optical and Spectroscopic Properties for Gold Nanoparticles. *J. Phys. Chem. C* **2007**, *111* (40), 14664–14669.

(8) Saha, K.; Agasti, S. S.; Kim, C.; Li, X.; Rotello, V. M. Gold Nanoparticles in Chemical and Biological Sensing. *Chem. Rev.* **2012**, *112* (5), 2739–2779.

(9) Marie-Christine Daniel and Didier Astruc. Gold Nanoparticles: Assembly, Supramolecular Chemistry, Quantum-Size-Related Properties, and Applications toward Biology, Catalysis, and Nanotechnology. *Chem. Rev.* **2004**, *104* (1), 293–346.

(10) Turkevich, J.; Stevenson, P. C.; Hillier, J. A Study of the Nucleation and Growth Processes in

the Synthesis of Colloidal Gold. *Discuss. Faraday Soc.* **1951**, *11* (c), 55.

(11) Philip, D. Synthesis and Spectroscopic Characterization of Gold Nanoparticles. *Spectrochim. Acta - Part A Mol. Biomol. Spectrosc.* **2008**, *71* (1), 80–85.

(12) Murphy, C. J.; Sau, T. K.; Gole, A. M.; Orendorff, C. J.; Gao, J.; Gou, L.; Hunyadi, S. E.; Li, T.; April, R. V; Final, I.; et al. Anisotropic Metal Nanoparticles : Synthesis , Assembly , and Optical Applications. **2005**, 13857–13870.

(13) Pattnaik, P. Surface Plasmon Resonance. *Appl. Biochem. Biotechnol.* **2005**, *126* (1), 79–92.

(14) Zhang, H.; Wang, D. Controlling the Growth of Charged-Nanoparticle Chains through Interparticle Electrostatic Repulsion. *Angew. Chemie Int. Ed.* **2008**, *47* (21), 3984–3987.

(15) Nightingale, E. R. Phenomenological Theory of Ion Solvation. Effective Radii of Hydrated Ions. *J. Phys. Chem.* **1959**, *63* (9), 1381–1387.

(16) Campi, E.; Ostacoli, G.; Meirone, M.; Saini, G. Stability of the Complexes of Tricarballylic and Citric Acids with Bivalent Metal Ions in Aqueous Solution. *J. Inorg. Nucl. Chem.* **1964**, *26* (4), 553–564.

(17) Li, N. C.; Lindenbaum, A.; White, J. M. Some Metal Complexes of Citric and Tricarballylic Acids. *J. Inorg. Nucl. Chem.* **1959**, *12* (1–2), 122–128.

(18) Wyrzykowski, D.; Chmurzyński, L. Thermodynamics of Citrate Complexation with Mn2+, Co2+, Ni2+ and Zn2+ Ions. *J. Therm. Anal. Calorim.* **2010**, *102* (1), 61–64.

(19) Pradeep, T.; Anshup. Noble Metal Nanoparticles for Water Purification: A Critical Review. *Thin Solid Films* **2009**, *517* (24), 6441–6478.

(20) Guruprasad, V. S.; Maheshwari, V. Magnetic Nano-Nets for Capture of Microbes in Solution Based on Physical Contact. *J. Colloid Interface Sci.* **2019**, *535*, 33–40.

(21) Martins, A.; Spengler, G.; Molnár, J.; Amaral, L. Bacterial Antibiotic Resistance. *eLS* **2014**, 1–

11.

(22) Stewart, P. S.; William Costerton, J. Antibiotic Resistance of Bacteria in Biofilms. *Lancet* **2001**, *358* (9276), 135–138.

(23) Banin, E.; Hughes, D.; Kuipers, O. P. Editorial: Bacterial Pathogens, Antibiotics and Antibiotic Resistance. *FEMS Microbiol. Rev.* **2017**, *41* (3), 450–452.

(24) Cohen, S. N.; Chang, A. C. Y.; Hsu, L. Nonchromosomal Antibiotic Resistance in Bacteria: Genetic Transformation of Escherichia Coli by R-Factor DNA. *Proc. Natl. Acad. Sci.* **1972**, *69* (8), 2110–2114.

(25) Elimelech, M. The Global Challenge for Adequate and Safe Water. *J. Water Supply Res. Technol. - AQUA* **2006**, *55* (1), 3–10.

(26) Onda, K.; Lobuglio, J.; Bartram, J. Global Access to Safe Water: Accounting for Water Quality and the Resulting Impact on MDG Progress. *Int. J. Environ. Res. Public Health* **2012**, *9* (3), 880–894.

(27) Damkjaer, S.; Taylor, R. The Measurement of Water Scarcity: Defining a Meaningful Indicator. *Ambio* **2017**, *46* (5), 513–531.

(28) Panáček, A.; Kvítek, L.; Prucek, R.; Kolář, M.; Večeřová, R.; Pizúrová, N.; Sharma, V. K.; Nevěčná, T.; Zbořil, R. Silver Colloid Nanoparticles: Synthesis, Characterization, and Their Antibacterial Activity. *J. Phys. Chem. B* **2006**, *110* (33), 16248–16253.

(29) Chen, C. Y.; Chiang, C. L. Preparation of Cotton Fibers with Antibacterial Silver Nanoparticles. *Mater. Lett.* **2008**, *62* (21–22), 3607–3609.

(30) Megiel, E. Surface Modification Using TEMPO and Its Derivatives. *Adv. Colloid Interface Sci.* **2017**, *250*, 158–184.

(31) Dogru, E.; Demirbas, A.; Altinsoy, B.; Duman, F.; Ocsoy, I. Formation of Matricaria Chamomilla Extract-Incorporated Ag Nanoparticles and Size-Dependent Enhanced

Antimicrobial Property. *J. Photochem. Photobiol. B Biol.* **2017**, *174* (July), 78–83.

(32) Lee, C.; Kim, J. Y.; Lee, W. Il; Nelson, K. L.; Yoon, J.; Sedlak, D. L. Supporting Information for Bactericidal Effect of Zero-Valent Iron Nanoparticles on Escherichia Coli in Aqueous Solution. *Environ. Sci. Technol.* **2008**, *8927*, 4927–4933.

(33) Diao, M.; Yao, M. Use of Zero-Valent Iron Nanoparticles in Inactivating Microbes. *Water Res.* **2009**, *43* (20), 5243–5251.

(34) Cui, Y.; Zhao, Y.; Tian, Y.; Zhang, W.; Lü, X.; Jiang, X. The Molecular Mechanism of Action of Bactericidal Gold Nanoparticles on Escherichia Coli. *Biomaterials* **2012**, *33* (7), 2327–2333.

(35) Khan, F. U.; Chen, Y.; Khan, N. U.; Ahmad, A.; Tahir, K.; Khan, Z. U. H.; Khan, A. U.; Khan, S. U.; Raza, M.; Wan, P. Visible Light Inactivation of E. Coli, Cytotoxicity and ROS Determination of Biochemically Capped Gold Nanoparticles. *Microb. Pathog.* **2017**, *107*, 419–424.

(36) Ali, Q.; Ahmed, W.; Lal, S.; Sen, T. Novel Multifunctional Carbon Nanotube Containing Silver and Iron Oxide Nanoparticles for Antimicrobial Applications in Water Treatment. *Mater. Today Proc.* **2017**, *4* (1), 57–64.

(37) Auffan, M.; Achouak, W.; Rose, J.; Roncato, M. A.; Chanéac, C.; Waite, D. T.; Masion, A.; Woicik, J. C.; Wiesner, M. R.; Bottero, J. Y. Relation between the Redox State of Iron-Based Nanoparticles and Their Cytotoxicity toward Escherichia Coli. *Environ. Sci. Technol.* **2008**, *42* (17), 6730–6735.

(38) Sadegh, H.; Ali, G. A. M.; Gupta, V. K.; Makhlouf, A. S. H.; Shahryari-ghoshekandi, R.; Nadagouda, M. N.; Sillanpää, M.; Megiel, E. The Role of Nanomaterials as Effective Adsorbents and Their Applications in Wastewater Treatment. *J. Nanostructure Chem.* **2017**.

(39) Li, P.; Li, J.; Wu, C.; Wu, Q.; Li, J. Synergistic Antibacterial Effects of β-Lactam Antibiotic Combined with Silver Nanoparticles. *Nanotechnology* **2005**, *16* (9), 1912–1917.

(40) Tran, N.; Hocquet, M.; Eon, B.; Sangwan, P.; Ratcliffe, J.; Hinton, T. M.; White, J.; Ozcelik, B.; Reynolds, N. P.; Muir, B. W. Non-Lamellar Lyotropic Liquid Crystalline Nanoparticles Enhance the Antibacterial Effects of Rifampicin against Staphylococcus Aureus. *J. Colloid Interface Sci.* **2018**, *519*, 107–118.

(41) Banoee, M.; Seif, S.; Nazari, Z. E.; Jafari-Fesharaki, P.; Shahverdi, H. R.; Moballegh, A.; Moghaddam, K. M.; Shahverdi, A. R. ZnO Nanoparticles Enhanced Antibacterial Activity of Ciprofloxacin against Staphylococcus Aureus and Escherichia Coli. *J. Biomed. Mater. Res. - Part B Appl. Biomater.* **2010**, *93* (2), 557–561.

(42) Panáček, A.; Kvítek, L.; Smékalová, M.; Večeřová, R.; Kolář, M.; Röderová, M.; Dyčka, F.; Šebela, M.; Prucek, R.; Tomanec, O.; et al. Bacterial Resistance to Silver Nanoparticles and How to Overcome It. *Nat. Nanotechnol.* **2018**, *13* (1), 65–71.

(43) Lantagne, D.; Rayner, J.; Mittelman, A.; Pennell, K. Comment on "a Re-Assessment of the Safety of Silver in Household Water Treatment: Rapid Systematic Review of Mammalian in Vivo Genotoxicity Studies." *Environ. Heal. A Glob. Access Sci. Source* **2017**, *16* (1), 1–9.

(44) Reddy, U. A.; Prabhakar, P. V.; Mahboob, M. Biomarkers of Oxidative Stress for in Vivo Assessment of Toxicological Effects of Iron Oxide Nanoparticles. *Saudi J. Biol. Sci.* **2017**, *24* (6), 1172–1180.

(45) Wang, L.; Dang, Z. M. Carbon Nanotube Composites with High Dielectric Constant at Low Percolation Threshold. *Appl. Phys. Lett.* **2005**, *87* (4), 2003–2006.

(46) Li, J.; Ma, P. C.; Chow, W. S.; To, C. K.; Tang, B. Z.; Kim, J. K. Correlations between Percolation Threshold, Dispersion State, and Aspect Ratio of Carbon Nanotubes. *Adv. Funct. Mater.* **2007**, *17* (16), 3207–3215.

(47) Gojny, F. H.; Wichmann, M. H. G.; Fiedler, B.; Kinloch, I. A.; Bauhofer, W.; Windle, A. H.; Schulte, K. Evaluation and Identification of Electrical and Thermal Conduction Mechanisms in

Carbon Nanotube/Epoxy Composites. *Polymer (Guildf).* **2006**, *47* (6), 2036–2045.

(48) Sanada, K.; Tada, Y.; Shindo, Y. Thermal Conductivity of Polymer Composites with Close-Packed Structure of Nano and Micro Fillers. *Compos. Part A Appl. Sci. Manuf.* **2009**, *40* (6–7), 724–730.

(49) Kimling, J.; Maier, M.; Okenve, B.; Kotaidis, V.; Ballot, H.; Plech, A. Turkevich Method for Gold Nanoparticle Synthesis Revisited. *J. Phys. Chem. B* **2006**, *110* (32), 15700–15707.

(50) Maheshwari, V.; Kane, J.; Saraf, R. F. Self-Assembly of a Micrometers-Long One-Dimensional Network of Cemented Au Nanoparticles. *Adv. Mater.* **2008**, *20* (2), 284–287.

(51) Yoosaf, K.; Ipe, B. I.; Suresh, C. H.; Thomas, K. G. In Situ Synthesis of Metal Nanoparticles and Selective Naked-Eye Detection of Lead Ions from Aqueous Media. *J. Phys. Chem. C* **2007**, *111* (34), 12839–12847.

(52) Hong, M.; Wu, L.; Tian, L.; Zhu, J. Controlled Assembly of Au, Ag, and Pt Nanoparticles with Chitosan. *Chem. - A Eur. J.* **2009**, *15* (24), 5935–5941.

(53) Hu, C.; Lin, K.; Wang, X.; Liu, S.; Yi, J.; Tian, Y.; Wu, B.; Chen, G.; Yang, H.; Dai, Y.; et al. Electrostatic Self-Assembling Formation of Pd Superlattice Nanowires from Surfactant-Free Ultrathin Pd Nanosheets. *J. Am. Chem. Soc.* **2014**, *136* (37), 12856–12859.

(54) Drbohlavova, J.; Hrdy, R.; Adam, V.; Kizek, R.; Schneeweiss, O.; Hubalek, J. Preparation and Properties of Various Magnetic Nanoparticles. *Sensors* **2009**, *9* (4), 2352–2362.

(55) Sahoo, S. K.; Agarwal, K.; Singh, A. K.; Polke, B. G.; Raha, K. C. 2010 Characterization of γ- and α-Fe2O3 Nano Powders Synthesized by Emulsion (2).Pdf. **2010**, *2* (8), 118–126.

(56) Wang, G.; Ling, Y.; Wheeler, D. A.; George, K. E. N.; Horsley, K.; Heske, C.; Zhang, J. Z.; Li, Y. Facile Synthesis of Highly Photoactive α-Fe2O3-Based Films for Water Oxidation. *Nano Lett.* **2011**, *11* (8), 3503–3509.

(57) Fujii, T.; de Groot, F. M. F.; Sawatzky, G. A.; Voogt, F. C.; Hibma, T.; Okada, K. In Situ XPS

Analysis of Various Iron Oxide Films Grown by NO 2 -Assisted Molecular-Beam Epitaxy. *Phys. Rev. B* **1999**, *59* (4), 3195–3202.

(58) McCafferty, E.; Wightman, J. P. Determination of the Concentration of Surface Hydroxyl Groups on Metal Oxide Films by a Quantitative XPS Method. *Surf. Interface Anal.* **1998**, *26* (8), 549–564.

(59) Lu, X.; Wang, G.; Zhai, T.; Yu, M.; Gan, J.; Tong, Y.; Li, Y. Hydrogenated TiO 2 Nanotube Arrays for Supercapacitors. *Nano Lett.* **2012**, *12* (3), 1690–1696.

(60) Jana, N. R.; Gearheart, L.; Murphy, C. J. Wet Chemical Synthesis of High Aspect Ratio Cylindrical Gold Nanorods. *J. Phys. Chem. B* **2001**, *105* (19), 4065–4067.

(61) Pu, L.; Baig, M.; Maheshwari, V. Nanoparticle Chains as Electrochemical Sensors and Electrodes. *Anal. Bioanal. Chem.* **2016**, *408* (11), 2697–2705.

(62) Luo, J.; Jiang, S.; Zhang, H.; Jiang, J.; Liu, X. A Novel Non-Enzymatic Glucose Sensor Based on Cu Nanoparticle Modified Graphene Sheets Electrode. *Anal. Chim. Acta* **2012**, *709*, 47–53.

(63) Wang, Y.; Teng, X.; Wang, J. S.; Yang, H. Solvent-Free Atom Transfer Radical Polymerization in the Synthesis of Fe2O3@polystyrene Core-Shell Nanoparticles. *Nano Lett.* **2003**, *3* (6), 789–793.

(64) Tam, J.; Salgado, S.; Miltenburg, M.; Maheshwari, V. Electrochemical Synthesis on Single Cells as Templates. *Chem. Commun.* **2013**, *49* (77), 8641–8643.

(65) Krystosiak, P.; Tomaszewski, W.; Megiel, E. High-Density Polystyrene-Grafted Silver Nanoparticles and Their Use in the Preparation of Nanocomposites with Antibacterial Properties. *J. Colloid Interface Sci.* **2017**, *498*, 9–21.

(66) Dang, Z. M.; Shehzad, K.; Zha, J. W.; Mujahid, A.; Hussain, T.; Nie, J.; Shi, C. Y. Complementary Percolation Characteristics of Carbon Fillers Based Electrically Percolative Thermoplastic Elastomer Composites. *Compos. Sci. Technol.* **2011**, *72* (1), 28–35.

(67) Li, Q.; Mahendra, S.; Lyon, D. Y.; Brunet, L.; Liga, M. V.; Li, D.; Alvarez, P. J. J. Antimicrobial Nanomaterials for Water Disinfection and Microbial Control: Potential Applications and Implications. *Water Res.* **2008**, *42* (18), 4591–4602.

(68) Wu, X.; Lu, Y.; Zhou, S.; Chen, L.; Xu, B. Impact of Climate Change on Human Infectious Diseases: Empirical Evidence and Human Adaptation. *Environ. Int.* **2016**, *86*, 14–23.

(69) Delpla, I.; Jung, A. V.; Baures, E.; Clement, M.; Thomas, O. Impacts of Climate Change on Surface Water Quality in Relation to Drinking Water Production. *Environment International*. 2009.

(70) Yeo, B. S.; Bell, A. T. Enhanced Activity of Gold-Supported Cobalt Oxide for the Electrochemical Evolution of Oxygen. *J. Am. Chem. Soc.* **2011**, *133* (14), 5587–5593.

(71) Khan, S. U. M. Efficient Photochemical Water Splitting by a Chemically Modified N-TiO2. *Science (80-.).* **2002**, *297* (5590), 2243–2245.

(72) Esswein, A. J.; McMurdo, M. J.; Ross, P. N.; Bell, A. T.; Tilley, T. D. Size-Dependent Activity of Co 3 O 4 Nanoparticle Anodes for Alkaline Water Electrolysis. *J. Phys. Chem. C* **2009**, *113* (33), 15068–15072.

(73) Cheng, Y.; Jiang, S. P. Advances in Electrocatalysts for Oxygen Evolution Reaction of Water Electrolysis-from Metal Oxides to Carbon Nanotubes. *Prog. Nat. Sci. Mater. Int.* **2015**, *25* (6), 545–553.

(74) Lee, Y.; Suntivich, J.; May, K. J.; Perry, E. E.; Shao-Horn, Y. Synthesis and Activities of Rutile IrO 2 and RuO 2 Nanoparticles for Oxygen Evolution in Acid and Alkaline Solutions. *J. Phys. Chem. Lett.* **2012**, *3* (3), 399–404.

(75) Gorlin, Y.; Jaramillo, T. F. A Bifunctional Nonprecious Metal Catalyst for Oxygen Reduction and Water Oxidation. *J. Am. Chem. Soc.* **2010**, *132* (39), 13612–13614.

(76) Gong, M.; Li, Y.; Wang, H.; Liang, Y.; Wu, J. Z.; Zhou, J.; Wang, J.; Regier, T.; Wei, F.; Dai,

H. An Advanced Ni–Fe Layered Double Hydroxide Electrocatalyst for Water Oxidation. *J. Am. Chem. Soc.* **2013**, *135* (23), 8452–8455.

(77) Gong, M.; Dai, H. A Mini Review of NiFe-Based Materials as Highly Active Oxygen Evolution Reaction Electrocatalysts. *Nano Res.* **2015**, *8* (1), 23–39.

(78) Yang, Y.; Fei, H.; Ruan, G.; Xiang, C.; Tour, J. M. Efficient Electrocatalytic Oxygen Evolution on Amorphous Nickel–Cobalt Binary Oxide Nanoporous Layers. *ACS Nano* **2014**, *8* (9), 9518–9523.

(79) Kundu, S.; Jayachandran, M. Shape-Selective Synthesis of Non-Micellar Cobalt Oxide (CoO) Nanomaterials by Microwave Irradiations. *J. Nanoparticle Res.* **2013**, *15* (4), 1543.

(80) Petitto, S. C.; Marsh, E. M.; Carson, G. A.; Langell, M. A. Cobalt Oxide Surface Chemistry: The Interaction of CoO(100), Co3O4(110) and Co3O4(111) with Oxygen and Water. *J. Mol. Catal. A Chem.* **2008**, *281* (1–2), 49–58.

(81) Xiong, S.; Yuan, C.; Zhang, X.; Xi, B.; Qian, Y. Controllable Synthesis of Mesoporous Co 3 O 4 Nanostructures with Tunable Morphology for Application in Supercapacitors. *Chem. - A Eur. J.* **2009**, *15* (21), 5320–5326.

(82) Lu, X.; Ng, Y. H.; Zhao, C. Gold Nanoparticles Embedded within Mesoporous Cobalt Oxide Enhance Electrochemical Oxygen Evolution. *ChemSusChem* **2014**, *7* (1), 82–86.

(83) Tüysüz, H.; Hwang, Y. J.; Khan, S. B.; Asiri, A. M.; Yang, P. Mesoporous Co3O4 as an Electrocatalyst for Water Oxidation. *Nano Res.* **2013**, *6* (1), 47–54.